CHALMERS

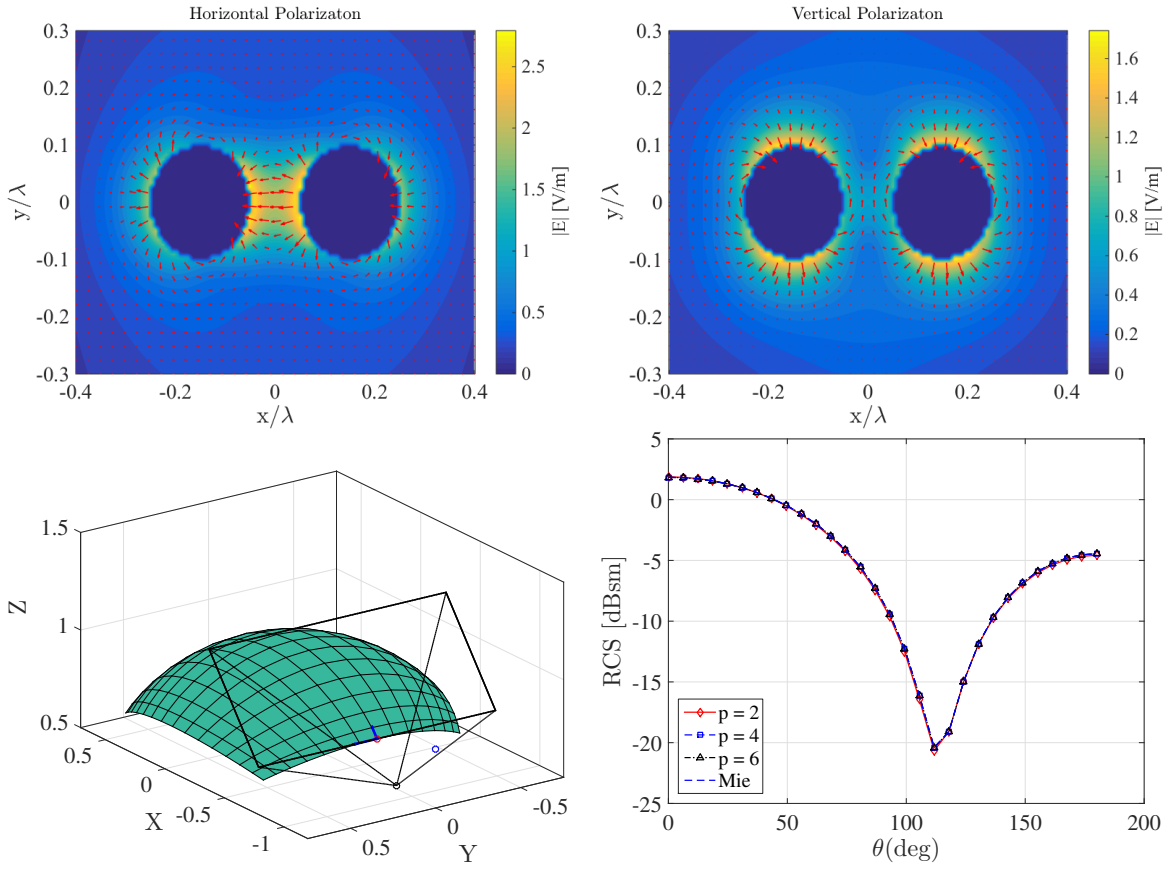

Method of Moments for Maxwell's equations based on higher-order interpolatory representation of geometry and currents

MAGNUS CARLSSON

Department of Signals and Systems
Chalmers University of Technology
Gothenburg, Sweden 2016

Master's thesis EX066/2016

Method of Moments for Maxwell's equations based on higher-order interpolatory representation of geometry and currents

MAGNUS CARLSSON

CHALMERS

Department of Signals and Systems
Division of Signal processing and Biomedical engineering
Chalmers University of Technology
Gothenburg, Sweden 2016

Method of Moments for Maxwell's equations based on higher-order interpolatory representation of geometry and currents
MAGNUS CARLSSON

Supervisor and Examiner: Thomas Rylander, Department of Signals and Systems
Co-supervisor: Johan Winges

Master's Thesis EX066/2016
Department of Signals and Systems
Division of Signal processing and Biomedical engineering
Chalmers University of Technology
412 96 Gothenburg
Telephone +46 31 772 1000

Cover: Upper left: Electric near field around two PEC sphere with incident horizontal light.
Upper right: Electric near field around the PEC sphere with incident vertical light.
Down left: A curved surface element with a first-order Taylor approximation of the surface.
Down right: A Radar Cross-Section spectrum as a function on incident polar angle for a PEC sphere.

Typeset in LaTeX
Gothenburg, Sweden 2016

Abstract

Electromagnetic scattering is a widely explored field in science and engineering, where a vast number of applications can be found in the open litterature. The Method of Moments (MoM) is an efficient numerical techniuqe for solving scattering problems. This thesis explores the combination of a collocation scheme and the usage of higher-order divergence-conforming basis functions for the currents induced on the scatterer. The problem of a perfect electric conducting (PEC) sphere is analyzed and the numerical results are in good agreement with analytical solutions. Exponential convergence in the polynomial order p of the current expansion is achieved for $p \leq 6$. In addition, two adjacent PEC spheres are analyzed for an incident plane wave with (i) the electric field polarized along the straight line between the centers of the spheres and (ii) the electric field polarized perpendicular to the straight line between the centers of the spheres.

Acknowledgement

This thesis is the concluding part of the Master's Program in Applied Physics at Chalmers University of Technology. The thesis work has been conducted at the department of Signals and Systems at Chalmers University of Technology during autumn 2015 and beginning of spring 2016.

I would like to express my gratitude to everyone that in some way has contributed to this thesis, and especially to the following persons:

Assoc. Prof. Thomas Rylander, my supervisor and examiner, for making this thesis possible, for his great dedication in this work and for all the interesting and inspiring discussions.

Assoc. Prof. Matthys Botha, for his contribution to the treatment of Singular integrals and his great knowledge and guidance in the Method of Moments.

Johan Winges, for guidance, support, interesting discussions and for his contribution to the programming part of this thesis.

Göteborg, April 2016
Magnus Carlsson

Notations

$\boldsymbol{E}$	Electric field (V/m)
$\boldsymbol{D}$	Electric flux density (C/m^2)
$\boldsymbol{H}$	Magnetic field (A/m)
$\boldsymbol{B}$	Magnetic flux density (T)
$\boldsymbol{J}$	Electric current density (A/m^2)
$\boldsymbol{M}$	Magnetic current density (V/m^2)
$\boldsymbol{A}$	Magnetic vector potenial (Vs/m)
$\boldsymbol{F}$	Electric vector potenial (VF/m)
ϕ_e	Electric potential (V)
ϕ_m	Magnetic potential (A)
ρ	Electric charge density (C/m^3)
ϱ	Magnetic charge density (T/m)
ω	Angular frequency (rad/s)
ϵ	Permittivity (F/m)
μ	Permeability (H/m)
j	Imaginary unit

Contents

Chapter 1

Introduction

Electromagnetic scattering caused by physical objects is a frequently occurring topic in engineering and science. In radar [1,2] applications, the object may be an airplane or a ship and significant scattering is often caused by metallic conductors that are part of the construction. A possible interest could be to improve the stealth properties [3, 4] of these objects. This could be achieved by investigating the radar cross section (RCS) of the object. In other cases, such as light scattering from metallic nanoparticles, plasmonic resonances [5, 6] occurs at certain frequencies. At these frequencies, the scattering objects may change absorbing and transmitting spectra dramatically.

To gain a deeper understanding of the previously mentioned topics, the theory of electromagnetic scattering needs to be exploited. In practice, numerical methods are needed since analytic solutions are very complicated or impossible to derive. The Method of Moments (MoM) is an attractive technique used to solve electromagnetic scattering problems in the frequency domain and it is the topic of this work. In the following chapters, the theory of MoM is outlined and applied on a canonical test case, namely the scattering of a perfect conducting sphere (PEC) sphere.

1.1 Maxwell's equations

Maxwell's equations describe the phenomena of classical electromagnetics, which in the frequency domain are

$$\nabla \times \boldsymbol{E} = -\boldsymbol{M} - j\omega \boldsymbol{B}, \tag{1.1}$$

$$\nabla \times \boldsymbol{H} = \boldsymbol{J} + j\omega \boldsymbol{D}, \tag{1.2}$$

$$\nabla \cdot \boldsymbol{D} = \rho, \tag{1.3}$$

$$\nabla \cdot \boldsymbol{B} = \varrho, \tag{1.4}$$

where we assume harmonic time dependence of the fields: $\boldsymbol{E}(\boldsymbol{r}, t) = \mathrm{Re}[\boldsymbol{E}(\boldsymbol{r})e^{j\omega t}]$, $\boldsymbol{H}(\boldsymbol{r}, t) = \mathrm{Re}[\boldsymbol{H}(\boldsymbol{r})e^{j\omega t}]$. The time dependence $e^{j\omega t}$ is supressed throughout this thesis.

In equations (1.1) - (1.4), $\boldsymbol{E}$ is the electric field, $\boldsymbol{B}$ is the magnetic flux density, $\boldsymbol{H}$ is the magnetic field, $\boldsymbol{D}$ is the displacement field, $\boldsymbol{J}$ is the electric current density and ρ is the electric charge density. The magnetic current density $\boldsymbol{M}$ and charge density ϱ are not physically realizable quantities but are useful mathematical tools in solving radiation and scattering problems.

The continuity equation for electric and magnetic charge are,

$$j\omega\rho + \nabla \cdot \boldsymbol{J} = 0, \tag{1.5}$$

$$j\omega\varrho + \nabla \cdot \boldsymbol{M} = 0. \tag{1.6}$$

This follows from taking the divergence of equations (1.1)-(1.2) and combining with equations (1.3)-(1.4).

In this thesis, we restrict our attention to *linear* and *isotropic* materials. For such materials, the consitutive relations are

$$\boldsymbol{B} = \mu\boldsymbol{H}, \tag{1.7}$$

$$\boldsymbol{D} = \epsilon\boldsymbol{E}, \tag{1.8}$$

where ϵ is the electric permittivity and μ is the magnetic permeability for the specific material that is considered.

1.1.1 Boundary conditions at interfaces between different media

Consider two regions, V_1 and V_2, separated by the surface interface S. Let the normal vector $\hat{\boldsymbol{n}}_2$ be perpendicular to S such that it points into V_1. On the interface S, we have the boundary conditions

$$\hat{\boldsymbol{n}}_2 \times (\boldsymbol{E}_1 - \boldsymbol{E}_2) = -\boldsymbol{M}_{\mathrm{s}}, \tag{1.9}$$

$$\hat{\boldsymbol{n}}_2 \times (\boldsymbol{H}_1 - \boldsymbol{H}_2) = \boldsymbol{J}_{\mathrm{s}}, \tag{1.10}$$

$$\hat{\boldsymbol{n}}_2 \cdot (\boldsymbol{D}_1 - \boldsymbol{D}_2) = \rho_{\mathrm{s}}, \tag{1.11}$$

$$\hat{\boldsymbol{n}}_2 \cdot (\boldsymbol{B}_1 - \boldsymbol{B}_2) = \varrho_{\mathrm{s}}, \tag{1.12}$$

where the surface current and charge densities coincide with the interface S between V_1 and V_2. Equations (1.9) and (1.10) state the discontinuity in the tangential parts of $\boldsymbol{H}$ and $\boldsymbol{E}$ at the interface between the two regions are equal to the surface current densities at the interface. Equations (1.11) and (1.12) state similary that the discontinuity between the normal components of $\boldsymbol{D}$ and $\boldsymbol{B}$ are equal to the surface charge densities at the interface.

If V_2 is a perfect electric conductor (PEC) and V_1 is a dielectric, the boundary conditions reduce to

$$\hat{\boldsymbol{n}}_2 \times \boldsymbol{E}_1 = 0, \tag{1.13}$$

$$\hat{\boldsymbol{n}}_2 \times \boldsymbol{H}_1 = \boldsymbol{J}_\mathrm{s}, \tag{1.14}$$

$$\hat{\boldsymbol{n}}_2 \cdot \boldsymbol{D}_1 = \rho_\mathrm{s}, \tag{1.15}$$

$$\hat{\boldsymbol{n}}_2 \cdot \boldsymbol{B}_1 = 0, \tag{1.16}$$

since all the fields inside the PEC are zero at non-zero frequency. The PEC boundary conditions are a very good approximation for metallic surfaces in the microwave regime.

1.2 Integral representations of the electromagnetic fields

In the following section, we rewrite Maxwell's equaitons (1.1) - (1.4) as integral equations, where the scattered fields $\boldsymbol{E}^\mathrm{s}$ and $\boldsymbol{H}^\mathrm{s}$ may be expressed as functions of the induced surface currents $\boldsymbol{J}_\mathrm{s}$ and $\boldsymbol{M}_\mathrm{s}$ on the scatterer. This is done by introducing so-called *Green's functions*.

We illustrate this procedure in the context of electrostatics [7]. Consider the inhomogeneus differential scalar Poisson's equation

$$\nabla^2 \phi = -\frac{\rho}{\epsilon_0}, \tag{1.17}$$

for the electric potential ϕ. For a system of n point charges q_i located at $\boldsymbol{r}_i'$, with $i = 1, 2, ..., n$, the charge density can be expressed as

$$\rho = \sum_{i=1}^{n} q_i \delta^3(\boldsymbol{r} - \boldsymbol{r}_i'). \tag{1.18}$$

The solution of Poisson's equation (1.17) at $\boldsymbol{r}$ in free space can be constructed by superposition:

$$\phi(\boldsymbol{r}) = \sum_{i=1}^{n} \frac{q_i}{4\pi\epsilon_0 |\boldsymbol{r} - \boldsymbol{r}_i'|}. \tag{1.19}$$

For a continuum charge density $\rho(\boldsymbol{r}')$, the sum is replaced by an intergral

$$\phi(\boldsymbol{r}) = \int_V \frac{\rho(\boldsymbol{r}')}{4\pi\epsilon_0 |\boldsymbol{r} - \boldsymbol{r}'|} \, \mathrm{d}V'. \tag{1.20}$$

It is possible to show that (1.20) and (1.17) are equivalent by applying the Laplace operator on both sides in (1.20). The resulting integrand is singular, but by noting that [7]

$$\nabla^2 \left(\frac{1}{|\boldsymbol{r} - \boldsymbol{r}'|} \right) = -4\pi\delta^3(\boldsymbol{r} - \boldsymbol{r}'), \tag{1.21}$$

we find the expressions are indeed equivalent. For this specific problem, we identify form (1.20) that the Green's function is

$$G(\boldsymbol{r}, \boldsymbol{r}') = \frac{1}{4\epsilon_0 \pi |\boldsymbol{r} - \boldsymbol{r}'|}, \tag{1.22}$$

which represents the potential or field at $\boldsymbol{r}$ produced by a point charge at $\boldsymbol{r}'$. Hence, the differential equation formulation (1.17) could be reformulated as an integral equation

$$\phi(\boldsymbol{r}) = \int_V G(\boldsymbol{r}, \boldsymbol{r}') \rho(\boldsymbol{r}') \, \mathrm{d}V', \tag{1.23}$$

where the objective is to compute the source distribution ρ given the field ϕ. This procedure can be generalized to include other physical situations. Consider a differential equation

$$D\left[f\right] = s, \tag{1.24}$$

where D is a differential operator, f is a scalar field (or a component of a vector field) and s is a scalar source distribution (or a component of a vector source distribution). The Green's function $G(\boldsymbol{r}, \boldsymbol{r}')$ represents the value of f at $\boldsymbol{r}$ due to a point source at $\boldsymbol{r}'$ and it satisfies

$$D\left[G(\boldsymbol{r}, \boldsymbol{r}')\right] = \delta^3(\boldsymbol{r} - \boldsymbol{r}'). \tag{1.25}$$

Multiplying (1.25) with $s(\boldsymbol{r}')$ and integrating with respect to $\boldsymbol{r}'$ yields

$$\int D\left[G(\boldsymbol{r}, \boldsymbol{r}') s(\boldsymbol{r}')\right] \mathrm{d}V' = \int \delta^3(\boldsymbol{r} - \boldsymbol{r}') s(\boldsymbol{r}') \, \mathrm{d}V'. \tag{1.26}$$

The right-hand side reduces to $s(\boldsymbol{r})$ due the nature of the Dirac distribution $\delta^3(\boldsymbol{r} - \boldsymbol{r}')$ and the left-hand side can be rewritten as

$$D\left[\int G(\boldsymbol{r}, \boldsymbol{r}') s(\boldsymbol{r}') \, \mathrm{d}V'\right], \tag{1.27}$$

due to the linearity of the differential operator. By comparison with (1.24), we can identify the integral formulation

$$f(\boldsymbol{r}) = \int G(\boldsymbol{r}, \boldsymbol{r}') s(\boldsymbol{r}') \, \mathrm{d}V', \tag{1.28}$$

of the initial differential formulation. It is clear that the integration domain in (1.28) reduces to the region where sources exist. This technique is thus very powerful for localized source distributions in an otherwise source-free region. This is often the case in scattering problems, where a relatively small metallic object scatters a field into free space. For conductors, the source currents are generally restricted to the surface of the conductor [8] and, thus, the sources are located only on the surface of the scatterer. In the following, we assume that there is only currents on the surface of the geometry and we denote the surface current densities by $\boldsymbol{J}$ and $\boldsymbol{M}$ to simplify the notation. The fields are computed at the obervation point $\boldsymbol{r}$ and the sources are located at $\boldsymbol{r}'$.

For homogeneous space with permittivity ϵ and permeability μ, the above procedure can be applied to find the integral equations for the scattered fields produced by the surface currents $\boldsymbol{J}$ and $\boldsymbol{M}$, where a detailed derivation can be found in [9]. The scattered fields $\boldsymbol{E}^{\mathrm{s}}$ and $\boldsymbol{H}^{\mathrm{s}}$ may be expressed as

$$\boldsymbol{E}^{\mathrm{s}} = -j\omega\boldsymbol{A} - \nabla\phi_{\mathrm{e}} - \frac{1}{\epsilon}\nabla \times \boldsymbol{F}, \tag{1.29}$$

$$\boldsymbol{H}^{\mathrm{s}} = -j\omega\boldsymbol{F} - \nabla\phi_{\mathrm{m}} + \frac{1}{\mu}\nabla \times \boldsymbol{A}, \tag{1.30}$$

where $\boldsymbol{A}$ and $\boldsymbol{F}$ are the magnetic and electric vector potentials, ϕ_{e} and ϕ_{m} are the electric and magnetic scalar potential, respectively. The expressions for these quantities are

$$\boldsymbol{A}(\boldsymbol{r}) = \mu \int_S \boldsymbol{J}(\boldsymbol{r}')G(\boldsymbol{r},\boldsymbol{r}')\,\mathrm{d}S', \tag{1.31}$$

$$\boldsymbol{F}(\boldsymbol{r}) = \epsilon \int_S \boldsymbol{M}(\boldsymbol{r}')G(\boldsymbol{r},\boldsymbol{r}')\,\mathrm{d}S', \tag{1.32}$$

$$\phi_e(\boldsymbol{r}) = \frac{1}{\epsilon}\int_S \rho(\boldsymbol{r}')G(\boldsymbol{r},\boldsymbol{r}')\,\mathrm{d}S', \tag{1.33}$$

$$\phi_m(\boldsymbol{r}) = \frac{1}{\mu}\int_S \varrho(\boldsymbol{r}')G(\boldsymbol{r},\boldsymbol{r}')\,\mathrm{d}S', \tag{1.34}$$

where $G(\boldsymbol{r},\boldsymbol{r}')$ is the dynamic Green's function in 3D for a homogeneous region that is unbounded and the integration is performed over the surface S of the conductor. The Green's function is

$$G(\boldsymbol{r},\boldsymbol{r}') = \frac{e^{-jkr}}{4\pi r}, \tag{1.35}$$

where $r = |\boldsymbol{r} - \boldsymbol{r}'|$ and $k = \omega\sqrt{\epsilon\mu}$. This Green's function is derived from the inhomogeneous Helmholtz equation

$$-\left(\nabla^2 f(\boldsymbol{r}) + k^2 f(\boldsymbol{r})\right) = s(\boldsymbol{r}). \tag{1.36}$$

The scattered fields may be expressed in terms of the linear operators $\mathcal{L}$ and $\mathcal{K}$ as sole functions of $\boldsymbol{J}$ and $\boldsymbol{M}$, by inserting (1.31) - (1.34) in (1.29) - (1.30) and using the expressions for the continuity of charge and current density (1.5) - (1.6), which yields

$$\boldsymbol{E}^{\mathrm{s}}(\boldsymbol{r}) = -j\omega\mu(\mathcal{L}\boldsymbol{J})(\boldsymbol{r}) - (\mathcal{K}\boldsymbol{M})(\boldsymbol{r}), \tag{1.37}$$

$$\boldsymbol{H}^{\mathrm{s}}(\boldsymbol{r}) = -j\omega\epsilon(\mathcal{L}\boldsymbol{M})(\boldsymbol{r}) + (\mathcal{K}\boldsymbol{J})(\boldsymbol{r}), \tag{1.38}$$

where the linear operators $\mathcal{L}$ and $\mathcal{K}$ are defined as

$$(\mathcal{L}\boldsymbol{X})(\boldsymbol{r}) = \left[1 + \frac{1}{k^2}\nabla\nabla\cdot\right]\int_S G(\boldsymbol{r},\boldsymbol{r}')\boldsymbol{X}(\boldsymbol{r}')\,\mathrm{d}S', \tag{1.39}$$

$$(\mathcal{K}\boldsymbol{X})(\boldsymbol{r}) = \nabla \times \int_S G(\boldsymbol{r},\boldsymbol{r}')\boldsymbol{X}(\boldsymbol{r}')\,\mathrm{d}S'. \tag{1.40}$$

The integral equations (1.37) and (1.38) are general expressions for the scattered fields. However, the scattered fields are usually divided into the *near-field* and *far-field* regions, where terms of different order $\mathcal{O}(r^n)$ are dominating.

1.2.1 Alternative representations (suitable for the near-field region)

The near-field region comprises the fields produced close to the sources. For field points that are close to the source distribution, alternative expressions of (1.39) and (1.40) may be used. The derivative operators are moved inside the integral signs, which yield

$$(\mathcal{L}\boldsymbol{X})(\boldsymbol{r}) = \int_S G(\boldsymbol{r},\boldsymbol{r}')\boldsymbol{X}(\boldsymbol{r}')\,\mathrm{d}S' + \frac{1}{k^2}\int_S \nabla\nabla\cdot[G(\boldsymbol{r},\boldsymbol{r}')\boldsymbol{X}(\boldsymbol{r}')]\,\mathrm{d}S', \tag{1.41}$$

$$(\mathcal{K}\boldsymbol{X})(\boldsymbol{r}) = \int_S \nabla\times[G(\boldsymbol{r},\boldsymbol{r}')\boldsymbol{X}(\boldsymbol{r}')]\,\mathrm{d}S', \tag{1.42}$$

where all derivatives are with respect to $\boldsymbol{r}$. Since $\boldsymbol{X}(\boldsymbol{r}')$ only depends on $\boldsymbol{r}'$, the derivatives only affects the Green's function. This yields terms that scale as $1/r, 1/r^2$ and $1/r^3$. Thus, the Green's function exhibits a singularity as the distance between source point and field tends to zero. Special care is neccesary for numerical integration of these terms as the results otherwise may become very inaccurate. Usually, the singularities are denoted as weak singularities ($1/r$), strong singularities ($1/r^2$) and hyper singularities ($1/r^3$). Special care is also taken if $\boldsymbol{r}$ and $\boldsymbol{r}'$ coincide exactly (true singularity) or are very close (near singularity).

Integration schemes designed to handle the near-field expressions can be found in the open literature for weak singularities [10] and for strong singularities [11]. Hyper singularities can be reduced to strong singularities by transferring one of the derivatives to the source. The second integral in (1.43) possess a hyper singularity, which after integration by parts [9] yields the operators

$$(\mathcal{L}\boldsymbol{X})(\boldsymbol{r}) = \int_S G(\boldsymbol{r},\boldsymbol{r}')\boldsymbol{X}(\boldsymbol{r}')\,\mathrm{d}S' + \frac{1}{k^2}\int_S \nabla G(\boldsymbol{r},\boldsymbol{r}')\nabla'\cdot\boldsymbol{X}(\boldsymbol{r}')\,\mathrm{d}S', \tag{1.43}$$

$$(\mathcal{K}\boldsymbol{X})(\boldsymbol{r}) = \int_S [\nabla G(\boldsymbol{r},\boldsymbol{r}')]\times\boldsymbol{X}(\boldsymbol{r}')\,\mathrm{d}S', \tag{1.44}$$

and the integration schemes for weak and strong singularities suffice. Here, the differation formula $\nabla\times(G\boldsymbol{X}) = \nabla G\times\boldsymbol{X}' + G\nabla\times\boldsymbol{X}' = \nabla G\times\boldsymbol{X}'$ is used for (1.44).

1.2.2 Far-field representations

When $\boldsymbol{r}$ is located sufficiently far away from $\boldsymbol{r}'$, we approximate $r = |\boldsymbol{r}-\boldsymbol{r}'|$ as [7]

$$r = \begin{cases} r - \hat{\boldsymbol{r}}\cdot\boldsymbol{r}' & \text{for phase variations} \\ r & \text{for amplitude variations} \end{cases}, \tag{1.45}$$

given the far-field conditions $r \gg d$, $r \gg \lambda$ and $r \gg kd^2$, where $d = \max|\boldsymbol{r}'|$ is the maximum extension of the scatterer and $\lambda = 2\pi/k$. Consider the expressions for the scattered fields in (1.37) and (1.38). When acting upon the Green's function with the differential operators, it produces terms in the fields that vary according to $1/r$, $1/r^2$ and $1/r^3$. In the far-field, only the fields that vary as $1/r$ have a significant

amplitude. In addition, the electromagnetic wave is transverse i.e. there are no field components along the direction of propagation. The far-field expressions for the $\mathcal{L}$- and $\mathcal{K}$-operators then reduce to

$$(\mathcal{L}\boldsymbol{X})(\boldsymbol{r}) = -\hat{\boldsymbol{r}} \times \hat{\boldsymbol{r}} \times \boldsymbol{P}(\hat{\boldsymbol{r}}) \frac{e^{-jkr}}{kr}, \tag{1.46}$$

$$(\mathcal{K}\boldsymbol{X})(\boldsymbol{r}) = -jk\hat{\boldsymbol{r}} \times \boldsymbol{P}(\hat{\boldsymbol{r}}) \frac{e^{-jkr}}{kr}, \tag{1.47}$$

where

$$\boldsymbol{P}(\hat{\boldsymbol{r}}) = \frac{k}{4\pi} \int_S e^{-jk\hat{\boldsymbol{r}}\cdot\hat{\boldsymbol{k}}} \boldsymbol{X}(\boldsymbol{r}') \, \mathrm{d}S', \tag{1.48}$$

is the spatial Fourier transform of the current density $\boldsymbol{X}$ evaluated in the coordinate $k\hat{\boldsymbol{r}}$. A detailed derivation of the far-field expressions is given in Appendix A.

1.2.3 Green's functions

The physical interpretation of the Green's function is the field at $\boldsymbol{r}$ caused by a unit point source at at $\boldsymbol{r}'$ [12]. Below, we provide a derivation of the dynamic Green's function and introduce the so-called dyadic Green's function.

More generally, it entered as an integral solution (1.28) of an initial differential equation (1.24). The derivation of the Green's function is based on that the solution can be expresses as the superposition of the contribution from many point sources, all weighted by $G(\boldsymbol{r}, \boldsymbol{r}')$.

Scalar Green's function

The scalar Green's function can be derived from

$$(\nabla^2 + k^2) G(\boldsymbol{r}, \boldsymbol{r}') = -\delta^3(\boldsymbol{r} - \boldsymbol{r}'). \tag{1.49}$$

where $G(\boldsymbol{r}, \boldsymbol{r}')$ is a solution to the inhomogeneous Helmholtz equation (1.36). Since we have assumed homogeneous space, $G(\boldsymbol{r}, \boldsymbol{r}')$ may only depend on the distance between the source and observation points $r = |\boldsymbol{r} - \boldsymbol{r}'|$. The Laplacian in spherical coordinates for a scalar field f is given by

$$\nabla^2 f = \frac{1}{r^2}\frac{\partial}{\partial r}\left(r^2 \frac{\partial f}{\partial r}\right) + \frac{1}{r^2 \sin\theta}\frac{\partial}{\partial \theta}\left(\sin\theta \frac{\partial f}{\partial \theta}\right) + \frac{1}{r^2 \sin^2\theta}\frac{\partial^2 f}{\partial \varphi}^2. \tag{1.50}$$

It is then possible to rewrite (1.49) as

$$\frac{1}{r^2}\frac{\mathrm{d}}{\mathrm{d}r}\left(r^2 \frac{\mathrm{d}G(r)}{\mathrm{d}r}\right) + k^2 G(r) = 0, \quad r > 0. \tag{1.51}$$

The solution of (1.51) may be found in [13] for example and has the form

$$G(r) = A\frac{e^{-jkr}}{r}, \tag{1.52}$$

where A is an arbitrary constant and we have assumed only outward traveling waves from the source. The constant may be determined by substituting (1.52) in (1.49) and integrate over a sphere with radius r_0, where we let r_0 tend to zero. The different terms evaluate to

$$\begin{aligned}\int_{r<r_0} \nabla^2 G \,\mathrm{d}V &= \oint_{r=r_0} \nabla G \cdot \hat{\boldsymbol{n}} \mathrm{d}S = 4\pi r_0^2 \hat{\boldsymbol{r}} \cdot \nabla G \\ &= -4\pi A r_0^2 \left(\frac{e^{-jkr_0}}{r_0^2} + jk \frac{e^{-jkr_0}}{r_0} \right) \\ \int_{r<r_0} k^2 G \,\mathrm{d}V &= 4\pi k^2 A \left[-\frac{1}{jk} r_0 e^{-jkr_0} + \frac{1}{k^2}(e^{-jkr_0} - 1) \right] \\ \int_{r<r_0} -\delta^3(r) \,\mathrm{d}V &= -1.\end{aligned}$$

By taking the limit $r_0 \to 0$, we find that $A = 1/4\pi$ and we finally get the scalar Green's function

$$G(\boldsymbol{r}, \boldsymbol{r}') = \frac{e^{-jkr}}{4\pi r}. \tag{1.53}$$

Dyadic Green's functions

The expressions for the scattered fields (1.43) and (1.44) may be used when the distance between the source and field point is sufficiently large. Since the derivatives are only acting on the unprimed coordinates they only act on the scalar Green's function $G(\boldsymbol{r}, \boldsymbol{r}')$. The result may be expressed in terms of dyadic Green's functions according to

$$\bar{\bar{G}}_{\mathcal{L}}(\boldsymbol{r}, \boldsymbol{r}') = \left[\bar{\bar{I}} + \frac{1}{k^2} \nabla\nabla \right] G(\boldsymbol{r}, \boldsymbol{r}'), \tag{1.54}$$

$$\bar{\bar{G}}_{\mathcal{K}}(\boldsymbol{r}, \boldsymbol{r}') = \nabla \times G(\boldsymbol{r}, \boldsymbol{r}'). \tag{1.55}$$

In this thesis, we perform the integrations in Cartesian coordinates. The dyadic Green's functions can then be expressed in matrix form and are given by

$$\bar{\bar{G}}_{\mathcal{L}}(\boldsymbol{r}, \boldsymbol{r}') = \begin{pmatrix} k^2 + \frac{\partial^2}{\partial x^2} & \frac{\partial^2}{\partial x \partial y} & \frac{\partial^2}{\partial x \partial z} \\ \frac{\partial^2}{\partial y \partial x} & k^2 + \frac{\partial^2}{\partial y^2} & \frac{\partial^2}{\partial y \partial z} \\ \frac{\partial^2}{\partial z \partial x} & \frac{\partial^2}{\partial z \partial y} & k^2 + \frac{\partial^2}{\partial x^2} \end{pmatrix} \frac{G(\boldsymbol{r}, \boldsymbol{r}')}{k^2}, \tag{1.56}$$

$$\bar{\bar{G}}_{\mathcal{K}}(\boldsymbol{r}, \boldsymbol{r}') = \begin{pmatrix} 0 & -\frac{\partial}{\partial z} & \frac{\partial}{\partial y} \\ \frac{\partial}{\partial z} & 0 & -\frac{\partial}{\partial x} \\ -\frac{\partial}{\partial y} & \frac{\partial}{\partial x} & 0 \end{pmatrix} G(\boldsymbol{r}, \boldsymbol{r}'). \tag{1.57}$$

The Green's function is then moved inside the matrix and the differentiations are calculated analytically. This operation is straightforward but algebraically tedious. The results are given below

$$\bar{\bar{G}}_{\mathcal{L}}(\boldsymbol{r},\boldsymbol{r}') = \begin{pmatrix} k^2+F_{xx} & F_{xy} & F_{xz} \\ F_{yx} & k^2+F_{yy} & F_{yz} \\ F_{zx} & F_{zy} & k^2+F_{zz} \end{pmatrix} \frac{G(\boldsymbol{r},\boldsymbol{r}')}{k^2}, \tag{1.58}$$

$$\bar{\bar{G}}_{\mathcal{K}}(\boldsymbol{r},\boldsymbol{r}') = \begin{pmatrix} 0 & -F_z & F_y \\ F_z & 0 & -F_x \\ -F_y & F_x & 0 \end{pmatrix} G(\boldsymbol{r},\boldsymbol{r}'), \tag{1.59}$$

where we use the following functions

$$F_m = \frac{(\xi_m - \xi_m')(-1-jkR)}{R^2}, \tag{1.60}$$

$$F_{mn} = \frac{(\xi_m - \xi_m')(\xi_n - \xi_n')(3(1+jkR) - k^2R^2)}{R^4}, \tag{1.61}$$

$$F_{mm} = \frac{3(\xi_m - \xi_m')^2}{R^4} + \frac{3jk(\xi_m - \xi_m')^2}{R^3} - \frac{1+k^2(\xi_m - \xi_m')^2}{R^2} - \frac{jk}{R}, \tag{1.62}$$

where $\xi_m, \xi_n = x, y$ or z. Inserting the expressions for the dyadic Green's function in (1.37) and (1.38) yield a compact notation

$$(\boldsymbol{\mathcal{L}X})(\boldsymbol{r}) = \int_S \bar{\bar{G}}_{\mathcal{L}}(\boldsymbol{r},\boldsymbol{r}')\boldsymbol{X}(\boldsymbol{r}')\,\mathrm{d}S', \tag{1.63}$$

$$(\mathcal{K}\boldsymbol{X})(\boldsymbol{r}) = \int_S \bar{\bar{G}}_{\mathcal{K}}(\boldsymbol{r},\boldsymbol{r}')\boldsymbol{X}(\boldsymbol{r}')\,\mathrm{d}S'. \tag{1.64}$$

Chapter 2

Method of Moments

The Method of Moments (MoM) is a technique to convert the integral equations decribed in Chapter 1 into a system of linear equations. It bears strong resemblance to the Finite Element Method (FEM), which is used to solve differential equations. To construct the set of linear equations, we use the *weighted residual method*, a general recipe for both the FEM and MoM.

For the MoM, the vector integral equations (1.37) and (1.38) have the form

$$L[\boldsymbol{X}] = \boldsymbol{V}, \tag{2.1}$$

where L denotes a linear integral operator, $\boldsymbol{V}$ is a given excitation function, and $\boldsymbol{X}$ is the unknown current distribution to be solved on the surface S. The surface S is discretized into elements, which for example may be triangles or quadrilaterals. The solution $\boldsymbol{X}$ is expanded in a linearly independent vector basis functions according to

$$\boldsymbol{X}(\boldsymbol{r}) \approx \sum_{j=1}^{N} X_j \boldsymbol{B}_j(\boldsymbol{r}), \tag{2.2}$$

where X_j are the unknown coefficients to be determined. The basis functions $\boldsymbol{B}_j(\boldsymbol{r})$ are low-order polynomials that are non-zero only in a few adjecent elements. We form the residual

$$\boldsymbol{r} = L[\boldsymbol{X}] - \boldsymbol{V}, \tag{2.3}$$

which we want to minimize. This may be done by introducing *weighting* functions $\boldsymbol{w}_i$ (as many as there are unknown coefficients) for weighting the residual (2.3). By enforcing the average of the weighted residual to be zero, i.e.

$$\int_S \boldsymbol{w}_i \cdot \boldsymbol{r} \, \mathrm{d}S = 0, \tag{2.4}$$

and inserting the expansion (2.2), we can solve for the unknown coefficients X_j

$$\sum_{j=1}^{N} X_j \int_S \boldsymbol{w}_i \cdot L[\boldsymbol{B}_j(\boldsymbol{r})] \, \mathrm{d}S = \int_S \boldsymbol{w}_i \cdot \boldsymbol{V} \, \mathrm{d}S. \tag{2.5}$$

Of particular importance is the choice of weighting functions $\boldsymbol{w}_i$. A common approach is to choose the weighting functions to be the same as the basis functions

$\boldsymbol{w}_i = \boldsymbol{B}_i$, which is referred to as Galerkin's method. Another approach is the so-called point matching method. It corresponds to taking the weighting functions as delta functions $\boldsymbol{w}_i = \delta^3(\boldsymbol{r} - \boldsymbol{r}_i)\boldsymbol{\xi}$, where $\boldsymbol{\xi}$ is a tangential vector to the surface. This choice enforces the residual to be zero at the matching points. The point matching method is exploited in this thesis.

2.1 Integral equations for PEC scatterers

The scattered fields are given by (1.37) and (1.38). We impose the boundary conditions on the PEC according to (1.13) and (1.14), where $\boldsymbol{E}$ and $\boldsymbol{H}$ are the total tangential fields on the surface. The total field is the superposition of the incoming and scattered field, where the scattered field is caused by the induced surface current on the scatterer

$$\hat{\boldsymbol{n}} \times (\boldsymbol{E}^{\mathrm{i}} + \boldsymbol{E}^{\mathrm{s}}(\boldsymbol{J})) = 0, \tag{2.6}$$

$$\hat{\boldsymbol{n}} \times (\boldsymbol{H}^{\mathrm{i}} + \boldsymbol{H}^{\mathrm{s}}(\boldsymbol{J})) = \boldsymbol{J}. \tag{2.7}$$

Equation (2.6) states that the total tangential electric field on the conductor must vanish on the surface. Likewise, (2.7) states that the total tangential magnetic field is related to the electric current. These boundary conditions may be enforced by scalar multiplying the total field with a tangential weighting function and integrate over the surface S according to

$$\int_S \boldsymbol{w}_i \cdot (\boldsymbol{E}^i + \boldsymbol{E}^s(\boldsymbol{J}))\,\mathrm{d}S = 0, \tag{2.8}$$

$$\int_S \boldsymbol{w}_i \cdot (\boldsymbol{H}^i + \boldsymbol{H}^s(\boldsymbol{J}))\,\mathrm{d}S = \int_S \boldsymbol{w}_i \cdot \boldsymbol{J}\,\mathrm{d}S. \tag{2.9}$$

We may then insert the expressions for the scattered fields in terms of the operators $\mathcal{L}$ and $\mathcal{K}$

$$\int_S \boldsymbol{w}_i \cdot (-j\omega\mu\mathcal{L}(\boldsymbol{J}))\,\mathrm{d}S = -\int_S \boldsymbol{w}_i \cdot \boldsymbol{E}^i\,\mathrm{d}S, \tag{2.10}$$

$$\int_S \boldsymbol{w}_i \cdot (\mathcal{K}(\boldsymbol{J}))\,\mathrm{d}S - \int_S \boldsymbol{w}_i \cdot \boldsymbol{J}\,\mathrm{d}S = -\int_S \boldsymbol{w}_i \cdot \boldsymbol{H}^i\,\mathrm{d}S, \tag{2.11}$$

where we have $\boldsymbol{M} = 0$, since we consider a PEC scatterer. Equation (2.10) is known as the electric field integral equation (EFIE) and (2.11) is known as the magnetic field integral equation (MFIE). Once $\boldsymbol{J}$ is determined by (2.10) or (2.11), the fields and other observable quantities associated with electromagnetic scattering can be computed.

We use the expansion in (2.2) to discretize the current according to the MoM. Inserting this expression in (2.10) and (2.11) yields a system of linear equations

$$\mathbf{Zi} = \mathbf{b}, \tag{2.12}$$

where the elements of the impedance matrices are given as

$$Z_{ij}^{\mathrm{EFIE}} = \int_S \boldsymbol{w}_i \cdot (-j\omega\mu\mathcal{L}(\boldsymbol{B}_j))\,\mathrm{d}S, \tag{2.13}$$

$$Z_{ij}^{\mathrm{MFIE}} = \int_S \boldsymbol{w}_i \cdot (\mathcal{K}(\boldsymbol{B}_j))\,\mathrm{d}S - \int_S \boldsymbol{w}_i \cdot \boldsymbol{B}_j\,\mathrm{d}S, \tag{2.14}$$

and the rows of the excitation vectors as

$$b_i^{EFIE} = -\int_S \boldsymbol{w}_i \cdot \boldsymbol{E}^i\,\mathrm{d}S, \tag{2.15}$$

$$b_i^{MFIE} = -\int_S \boldsymbol{w}_i \cdot \boldsymbol{H}^i\,\mathrm{d}S. \tag{2.16}$$

Once $\mathbf{Z}$ and $\mathbf{b}$ are assembled, the vector $\mathbf{i}$ of unknown coefficients may be obtained with matrix inversion.

On closed conductors, it is a well known problem that the EFIE and MFIE cannot produce unique solutions for all frequencies [8,9]. This corresponds to homogeneous solutions to these equations that satisfy the boundary conditions in the absense of an incoming field. These solutions are interior modes to the conductor and they produce a singular matrix $\mathbf{Z}$ at their resonance frequencies. A technique to avoid this problem is through a linear combination of the EFIE and the MFIE equations

$$\mathbf{Z}^{CFIE} = \alpha\mathbf{Z}^{EFIE} + (1-\alpha)Z_0\mathbf{Z}^{MFIE}, \tag{2.17}$$

$$\mathbf{b}^{CFIE} = \alpha\mathbf{b}^{EFIE} + (1-\alpha)Z_0\mathbf{b}^{MFIE} \tag{2.18}$$

where $\alpha \in [0,1]$ is a weighting parameter and this new scheme is called combined field integral equation (CFIE). Since the EFIE and MFIE have different internal resonance modes, α may be chosen to eliminate the singular behavior due to the internal resonances [8,9].

The incoming fields $\boldsymbol{E}^{\mathrm{i}}$ and $\boldsymbol{H}^{\mathrm{i}}$ are assumed to originate from sources very far away. Thus, the incident field can be approximated as a plane wave. The electric field of a plane wave propagating in $\hat{\boldsymbol{k}}$ direction has the form

$$\boldsymbol{E}^{\mathrm{i}} = \boldsymbol{E}_0 e^{-j\boldsymbol{k}\cdot\boldsymbol{r}},\ \boldsymbol{k} = \hat{\boldsymbol{k}}k, \tag{2.19}$$

where $\boldsymbol{r} = \hat{\boldsymbol{x}}x + \hat{\boldsymbol{y}}y + \hat{\boldsymbol{z}}z$ is the coordinate vector and $\boldsymbol{E}_0$ is a complex amplitude with a direction that lies in the plane perpendiculary to the direction of propagation $\hat{\boldsymbol{k}}$. Under the plane wave assumption, the magnetic field associated with the electric field (2.19) is obtained by

$$\boldsymbol{H}^{\mathrm{i}} = \frac{1}{Z}\hat{\boldsymbol{k}} \times \boldsymbol{E}^{\mathrm{i}}, \tag{2.20}$$

where $Z = \sqrt{\mu/\epsilon}$ is the impedance of the surrounding medium.

2.2 Representation of the geometry

In this thesis, we assume the geometry of interest has no sharp edges or corners. It is possible to include sharp edges or corners when formulating the EFIE and the MFIE equations but it is outside the scope of this thesis.

The surface of the geometry is discretized into curved quadrilateral cells, where the cells are also referred to as patches in the following. A quadratic approximation with 3×3 interpolatory nodes of a curved surface element S^e in shown in Fig. 2.1.

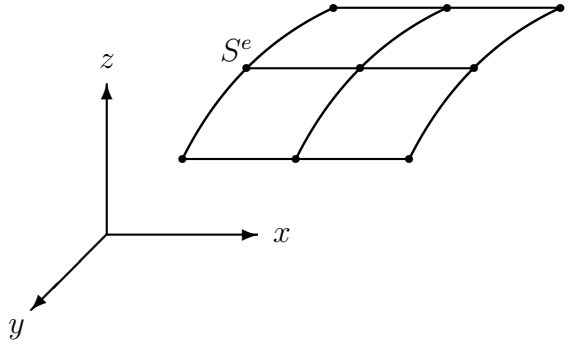

Figure 2.1: A curvelinear cell S^e in x-y-z space.

Each quadrilateral cell is described by a set of interpolatory nodes that coincide with the original geometry's surface. Another possibility to resolve the geometry is to use triangles instead of quadrilaterals. However, quadrilaterals are more suitable for numerical integration by means of product rules based on one-dimensional Gaussian quadrature rules.

2.2.1 Discretization of a sphere

A spherical scatterer of a homogeneous, isotropic and linear medium allows for analytical expressions on closed form that yield the scattered field given an incident plane wave. Thus, it is a simple but very interesting test case for scattering computations in electromagnetics. There are various ways to discretize the surface of a sphere and, in this thesis, we discretize the surface of a cube and map it onto the surface the sphere. Each face of the cube is discretized into rectangles, which yield curved patches on the sphere. Of course, the discretization of the cube influences the distribution of curved patches on the sphere.

It is easy and straightforward to discretize each face of the cube by a uniform and structured mesh of squares. Consider a cube centered at the origin. The coordinate vector of a point on the surface of the cube can be denoted $\boldsymbol{r}_\mathrm{c}$. The corresponding coordinate $\boldsymbol{r}_\mathrm{s}$ on the surface of a sphere with radius a can be obtained with the transformation

$$\boldsymbol{r}_\mathrm{s} = a\frac{\boldsymbol{r}_\mathrm{c}}{|\boldsymbol{r}_\mathrm{c}|}. \tag{2.21}$$

An example of this discretization is shown Figs. 2.2(a) and 2.2(b). Each face of the cube is discretized into 49 uniform sized squares and are then mapped to the sphere.

It is clear from Fig. 2.2(b) that the elements on the sphere are not uniform in size. This is because the patches near the center of each face are more streched than the patches along the edges. This may be a problem in the context of convergence studies with respect to the cell size. For such studies, it is desireable to preserve the uniformity in cell size on the spherical surface as the mesh is refined.

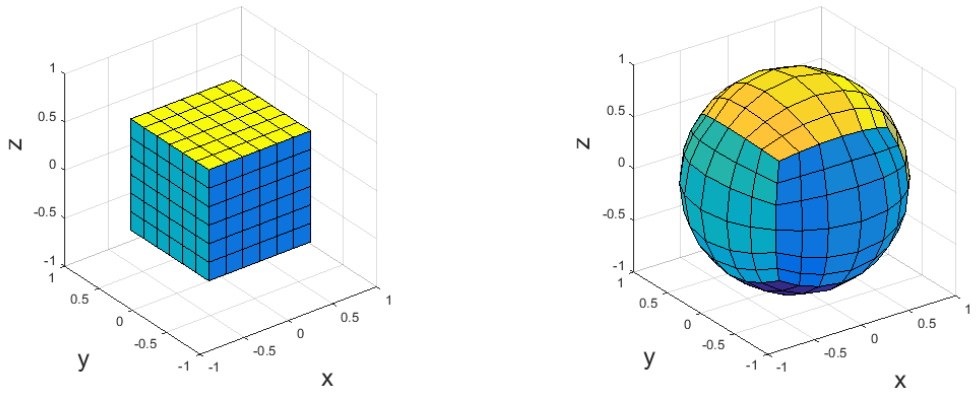

(a) Discretization of cube.

(b) Discretization of sphere.

Figure 2.2: Mapped discretization of cube to surface of sphere.

A method to alleviate this problem is to use an area preserving mapping from the cube to the sphere [14], by the means of inverse Lambert azimuthal equal area projection. An example mesh for the sphere, based on 49 cells on each face of the cube, is shown in Fig. 2.3.

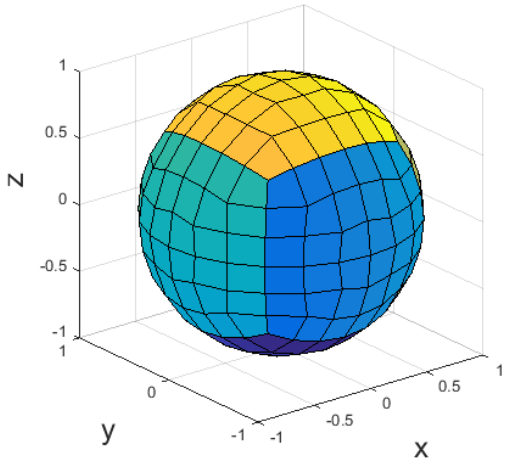

Figure 2.3: Area preserving mapping of cube to surface of sphere.

2.2.2 Reference element and higher-order mapping

An efficient framework to both describe and perform surface integration over an arbitrary surface element S^{e} in $\mathbb{R}^3$ Euclidian space is through the concept of a reference element. Consider the coordinate vector $\boldsymbol{r}$ in physical space (x, y, z) as a function of the reference element coordinates (u, v), which is expressed as

$$\boldsymbol{r}(u, v) = x(u, v)\hat{\boldsymbol{x}} + y(u, v)\hat{\boldsymbol{y}} + z(u, v)\hat{\boldsymbol{z}}. \tag{2.22}$$

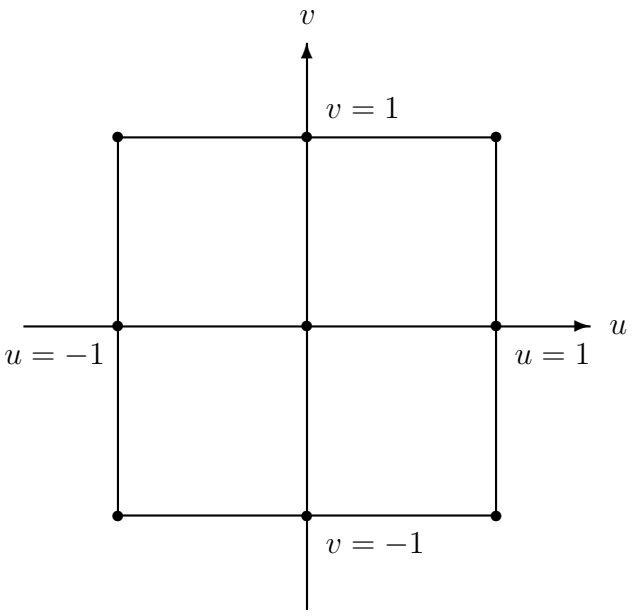

Figure 2.4: Integration limits of $[-1,1]^2$ cell.

To construct the mapping $\boldsymbol{r}(u,v)$, we use Lagrangian interpolation of the physical node coordinates $\boldsymbol{r}_{ij}$ according to

$$\boldsymbol{r}(u,v) = \sum_{i,j}^{M} \boldsymbol{r}_{ij} S_{ij}(u,v). \tag{2.23}$$

Here, we use a 2D Lagrangian polynomial $S_{ij}(u,v)$ by forming the product of two 1D polynomials $P_i^M(u)$ and $P_j^M(v)$ as

$$S_{ij}(u,v) = P_i^M(u)\, P_j^M(v),\ i,j = 1,2\ldots,M, \tag{2.24}$$

where the 1D Lagrangian polynomial of order $M-1$ is given by

$$P_i^M(u) = \prod_{j=1, j\neq i}^{M} \frac{u-u_j}{u_i-u_j}, \tag{2.25}$$

where $-1 \leq u \leq 1$ with u_j uniformly distributed on the interval $[-1,1]$ and

$$P_i^M(u_j) = \begin{cases} 1 & \text{if } i=j \\ 0 & \text{if } i\neq j \end{cases}. \tag{2.26}$$

Hence, we need to provide $M \times M$ nodes from each cell. It is also possible to calculate the derivatives $\{\frac{\partial x}{\partial u}, \frac{\partial x}{\partial v}, \frac{\partial y}{\partial u}, \frac{\partial y}{\partial v}, \frac{\partial z}{\partial u}, \frac{\partial z}{\partial v}\}$ from (2.23), which are used in the Jacobian matrix

$$\mathbf{J} = \begin{bmatrix} \frac{\partial x}{\partial u} & \frac{\partial y}{\partial u} & \frac{\partial z}{\partial u} \\ \frac{\partial x}{\partial v} & \frac{\partial y}{\partial v} & \frac{\partial z}{\partial v} \end{bmatrix}. \tag{2.27}$$

2.2.3 Co- and contravariant basis vectors

The covariant basis vectors $\boldsymbol{a}$ and $\boldsymbol{b}$ are tangential to the surface patch and they may be expressed as a function of u and v as

$$\begin{aligned} \boldsymbol{a} &= \frac{\partial \boldsymbol{r}}{\partial u} = \frac{\partial x}{\partial u}\hat{\boldsymbol{x}} + \frac{\partial y}{\partial u}\hat{\boldsymbol{y}} + \frac{\partial z}{\partial u}\hat{\boldsymbol{z}}, \\ \boldsymbol{b} &= \frac{\partial \boldsymbol{r}}{\partial v} = \frac{\partial x}{\partial v}\hat{\boldsymbol{x}} + \frac{\partial y}{\partial v}\hat{\boldsymbol{y}} + \frac{\partial z}{\partial v}\hat{\boldsymbol{z}}, \end{aligned} \tag{2.28}$$

where the derivatives are calculated from (2.23). If v is held constant and u is varied in (2.22), we get a curve on the surface and $\boldsymbol{a}$ is tangential to this curve. Similary, $\boldsymbol{b}$ is tangential to a curve where u is constant. The covariant basis vectors $\boldsymbol{a}$ and $\boldsymbol{b}$ are a suitable choice for representing the surface current in the MoM.

Next, we define the contravariant basis vectors by

$$\begin{aligned} \boldsymbol{\alpha} &= \nabla u = \frac{\partial u}{\partial x}\hat{\boldsymbol{x}} + \frac{\partial u}{\partial y}\hat{\boldsymbol{y}} + \frac{\partial u}{\partial z}\hat{\boldsymbol{z}}, \\ \boldsymbol{\beta} &= \nabla v = \frac{\partial v}{\partial z}\hat{\boldsymbol{x}} + \frac{\partial v}{\partial y}\hat{\boldsymbol{y}} + \frac{\partial v}{\partial z}\hat{\boldsymbol{z}}. \end{aligned} \tag{2.29}$$

The contravariant basis vectors are also tangential to the curved surface and, in addition, they are normal to constant-u or constant-v curves on the surface. It can be shown that (2.28) and (2.29) fullfill the orthogonality relations

$$\begin{aligned} \boldsymbol{a}\cdot\boldsymbol{\alpha} = 1, \quad \boldsymbol{b}\cdot\boldsymbol{\alpha} = 0, \\ \boldsymbol{a}\cdot\boldsymbol{\beta} = 0, \quad \boldsymbol{b}\cdot\boldsymbol{\beta} = 1. \end{aligned} \tag{2.30}$$

2.2.4 Surface integration

The surface integrals described in Chapter 1 are expressed in terms of an integration domain that extends over the entire surface S. To make use of the discretization in Section 2.2, an arbitrary integral of a function $f(\boldsymbol{r})$ over the surface S may be divided into a sum of integrals over the surface elements S^e according to

$$\int_S f(\boldsymbol{r})\,\mathrm{d}S = \sum_e \int_{S^e} f(\boldsymbol{r})\,\mathrm{d}S. \tag{2.31}$$

To integrate a quantity over a physical surface patch S^e, we use the mapping described by (2.23). If we make a change of variables to the reference space, we have to include the determinant of the Jacobian matrix of the mapping in the integration. It can be shown [15] that $|\boldsymbol{a}\times\boldsymbol{b}|$ corresponds to $\det\mathbf{J}$ for a 2D surface in 3D space and we use the notation $D(u,v) = |\boldsymbol{a}\times\boldsymbol{b}|$ in the following. Thus, a surface integral of a function $f(\boldsymbol{r})$ may be transformed to the reference cell in $u-v$ space according to

$$\int_{S^e} f(\boldsymbol{r})\,\mathrm{d}S = \int_{-1}^{1}\int_{-1}^{1} f(\boldsymbol{r}(u,v))D(u,v)\mathrm{d}u\mathrm{d}v. \tag{2.32}$$

The integral in the right-hand side of (2.32) can be calculated with numerical quadrature. Consider an integral of a function $f(x)$ over the interval $[-1, 1]$. A numerical quadrature rule of order N approximates the integral according to

$$\int_{-1}^{1} f(x)\,\mathrm{d}x \approx \sum_{p=1}^{N} f(x_p) w_p, \tag{2.33}$$

where w_p are weights and x_p are quadrature points associated with a specific quadrature rule. This can easily be extended to a 2D integral according to

$$\int_{-1}^{1}\int_{-1}^{1} f(u,v)\,\mathrm{d}u\mathrm{d}v \approx \sum_{p=1,q=1}^{N} f(u_p, v_q) w_p w_q. \tag{2.34}$$

In this thesis, we consider the Gauss-Legendre [16] and Gauss-Lobatto [17] quadrature schemes. It can be shown that Gauss-Legendre quadrature with N points provides the exact result if $f(x)$ is a polynomial of degree $2N-1$ or less. Similary, Gauss-Lobatto quadrature integrates exactly for polynomials of degree $2N-3$ or less. If $f(x)$ is not a polynomial function but infinitively differentiable at a real or complex number a, it can be expanded in Taylor series according to

$$f(x) = f(a) + \frac{f'(a)}{1!}(x-a) + \frac{f''(a)}{2!}(x-a)^2 + \frac{f'''(a)}{3!}(x-a)^3 + \ldots \tag{2.35}$$

where Gauss-Legendre quadrature evaluates the first $2N-1$ terms exactly. Similary, Gauss-Lobatto quadrature evaluates the first $2N-3$ terms exactly.

2.3 Representation of the current density

Next, we construct a representation of the current distribution flowing on the surface. One important physical consideration is the continuity equation for the current and charge distribution (1.5). This equation must also be fulfilled when moving over a cell boundary to an adjacent cell. This may be achieved by representing the current distribution in terms of *divergence-conforming* basis functions. A divergence-conforming basis function enforces continuity for the normal component of the vector field across cell egdes [15]. A divergence-conforming representation of the surface current yields a finite charge distribution for the entire surface. However, the charge distribution may be discontinuous along the edges of the cells.

A particular set of basis functions that satisfy these conditions are so-called Rao-Wilton-Glisson (RWG) functions [18], which are the lowest-order divergence-conforming basis functions. The RWG basis functions for triangle and quadrilateral cells can be found in [15].

2.3.1 Divergence conforming basis functions

The currents $\boldsymbol{J}$ and $\boldsymbol{M}$ are expanded according to (2.2). We may express the divergence-conforming basis function $\boldsymbol{B}_j$ in terms of basis functions formulated on the reference shown in Fig. 2.4, and then map those to the physical element in the

3D space (x, y, z). On the reference element, we construct the basis functions in terms of Lagrange polynomials as

$$\widetilde{\boldsymbol{B}}^U_{ij} = L^p_i(u) G^{p-1}_j(v) \hat{\boldsymbol{u}}, \tag{2.36}$$

$$\widetilde{\boldsymbol{B}}^V_{ij} = G^{p-1}_i(u) L^p_j(v) \hat{\boldsymbol{v}}, \tag{2.37}$$

where (i, j) are local indices, $L^p(u)$ is a Lagrange polynomial of order p with interpolatory points that coincide with the quadrature points of the Gauss-Lobatto integration scheme. Similary, $G^{p-1}(u)$ is a Lagrange polynomial of order $p-1$ with interpolatory points that coincide with the quadrature points of the Gauss-Legendre integration scheme. An example of the interpolatory degrees of freedom is shown in Figs. 2.5(a) for $\widetilde{\boldsymbol{B}}^U_{ij}$ and 2.5(b) for $\widetilde{\boldsymbol{B}}^V_{ij}$, where the order of the basis functions is $p = 2$.

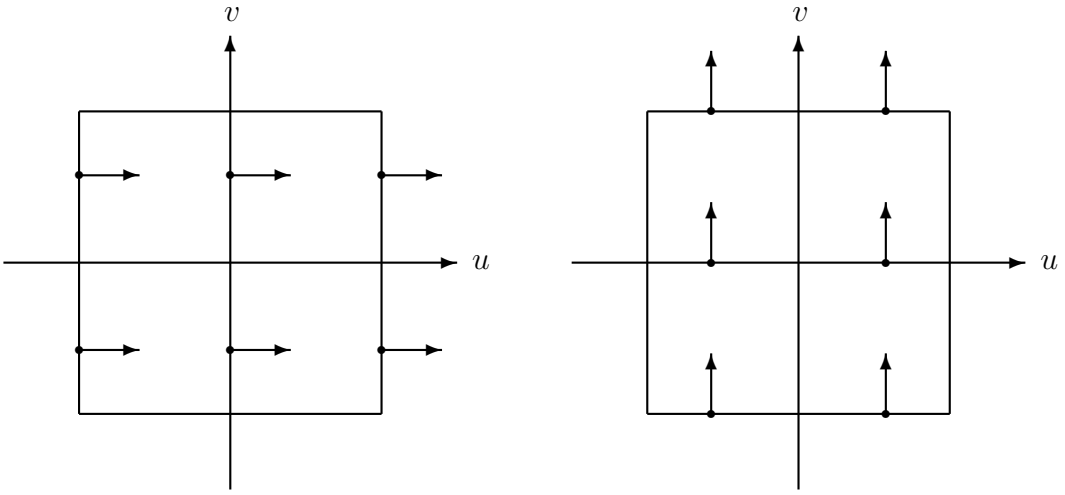

(a) $\widetilde{\boldsymbol{B}}^U_{ij} = L^3_i(u) G^2_j(v) \hat{\boldsymbol{u}}$ (b) $\widetilde{\boldsymbol{B}}^V_{ij} = G^2_i(u) L^3_j(v) \hat{\boldsymbol{v}}$

Figure 2.5: Interpolatory degrees of freedom for $\widetilde{\boldsymbol{B}}^U_{ij}$ (a) and $\widetilde{\boldsymbol{B}}^V_{ij}$ (b) shown on the reference element. Here, quadratic basis functions ($p = 2$) are shown.

We then need to map these functions to a specific element e. To account for the curvature of element e, it can be shown [8,15] that the relation between a divergence-conforming basis function $\widetilde{\boldsymbol{B}}_{ij}$ on the reference element and a divergence-conforming basis function $\boldsymbol{B}_{ij,e}$ on the physical element is given by

$$\boldsymbol{B}_{ij,e} = \frac{[\mathbf{J}^e]^T}{D^e} \widetilde{\boldsymbol{B}}_{ij}, \tag{2.38}$$

where $\mathbf{J}^e$ is given by Eq. (2.27) evaluated for element e. Equations (2.36) and (2.37) yield the basis functions expressed in physical space according to

$$\boldsymbol{B}^U_{ij,e} = \frac{1}{D^e(u, v)} L^p_i(u) G^{p-1}_j(v) \boldsymbol{a}_e, \tag{2.39}$$

$$\boldsymbol{B}^V_{ij,e} = \frac{1}{D^e(u, v)} G^{p-1}_i(u) L^p_j(v) \boldsymbol{b}_e, \tag{2.40}$$

where $\boldsymbol{a}_e$ and $\boldsymbol{b}_e$ are the covariant basis vectors evaluated for element e accodring to the expressions in Section 2.2.3. The global current $\boldsymbol{X}$ may then be expressed as a sum of basis functions multiplied with unknown coefficients

$$\boldsymbol{X}(\boldsymbol{r}) = \sum_e \left(\sum_{i,j} X^U_{ij,e} \boldsymbol{B}^U_{ij,e} + \sum_{i,j} X^V_{ij,e} \boldsymbol{B}^V_{ij,e} \right). \tag{2.41}$$

Each basis function associated with a corresponding degree of freedom that is interior the the element, i.e. does not coincide with its edges, is non-zero only on the element where it is defined. In case of an edge basis function, it is non-zero on the two adjacent elements that share the edge associated with the basis function. Thus, it is useful to define a global index $((i,j)_{\text{local}}, e) \mapsto j_{\text{global}}$ to relate the indices $(i,j)_{\text{local}}$ that are local to element e to the corresponding global basis function.

By expanding the current according to (2.41), one may simplify the calculation of integrals containing the dyadic Green's functions dramatically. Inserting (2.41) in either (1.63) or (1.64) yields

$$\sum_e \int_{S^e} \bar{\bar{G}}(\boldsymbol{r}, \boldsymbol{r}') \left(\sum_{i,j} X^U_{ij,e} \boldsymbol{B}^U_{ij,e}(\boldsymbol{r}') + \sum_{i,j} X^V_{ij,e} \boldsymbol{B}^V_{ij,e}(\boldsymbol{r}') \right) \mathrm{d}S'. \tag{2.42}$$

The integral over a patch S^e is mapped to the reference element and integrated numerically as described Section 2.2.4. With Eqs. (2.39) and (2.40) we arrive at

$$\begin{aligned} \sum_e \sum_{p,q} \Big[\bar{\bar{G}}(\boldsymbol{r}, \boldsymbol{r}'(u_p, v_q)) \Big(& \sum_{i,j} X^U_{ij,e} L^p_i(u_p) G^{p-1}_j(v_q) \boldsymbol{a}_e(u_p, v_q) + \\ & \sum_{i,j} X^V_{ij,e} G^{p-1}_i(u_p) L^p_j(v_q) \boldsymbol{b}_e(u_p, v_q) \Big) \Big] w_p w_q \end{aligned} \tag{2.43}$$

If we choose a quadrature scheme with quadrature points that coincide with the interpolation point for the vector basis function, i.e. a suitable product rule of Gauss-Legendre and Gauss-Lobatto quadrature, Eq.(2.43) simplifies to

$$\begin{aligned} \sum_e \Big(& \sum_{i,j} X^U_{ij,e} \bar{\bar{G}}(\boldsymbol{r}, \boldsymbol{r}'(u_i, v_j)) \boldsymbol{a}_e(u_i, v_j) w_i w_j + \\ & \sum_{i,j} X^V_{ij,e} \bar{\bar{G}}(\boldsymbol{r}, \boldsymbol{r}'(u_i, v_j)) \boldsymbol{b}_e(u_i, v_j) w_i w_j \Big), \end{aligned} \tag{2.44}$$

since basis functions satisfy the relations

$$\boldsymbol{B}_{ij,e} = \begin{cases} 1 & \text{if } i = p \text{ and } j = q \\ 0 & \text{otherwise} \end{cases}. \tag{2.45}$$

2.4 Weighting functions – Petrov-Galerkin's method

We use the Petrov-Galerkin's method and define the weighting functions

$$\boldsymbol{w}_i = C\delta^2(\boldsymbol{r} - \boldsymbol{r}_i)\boldsymbol{\xi} \tag{2.46}$$

where i is a global degree of freedom index, C is a normalizing constant to be determined and $\boldsymbol{\xi}$ is a contravariant basis vector to the surface, which is given by (2.29). The coordinate vector $\boldsymbol{r}_i$ is chosen to be collocated with the intepolation point for the corresponding degree of freedom $\boldsymbol{B}_i$. This way, the residual (2.3) is enforced to be zero at discrete points collocated with the degrees of freedom.

To find the constant C, we integrate the scalar part of the weighting function, i.e. $w_i = C\delta^2(\boldsymbol{r} - \boldsymbol{r}_i)$, over the surface. It is desirable to set this integral to unity

$$\int_S w_i \, \mathrm{d}S = 1, \tag{2.47}$$

for normalization purposes. Inserting the scalar part of (2.46) in (2.47), rewriting the integral to a sum over the elements e and transforming to the reference element yields

$$\sum_e \int_{-1}^{1} \int_{-1}^{1} C\delta^2(\boldsymbol{r}(u,v) - \boldsymbol{r}(u_i, v_i)) D^e(u,v) \mathrm{d}u\mathrm{d}v. \tag{2.48}$$

This evaluates to

$$CD^e(u_i, v_i) = 1 \Rightarrow C = \frac{1}{D^e(u_i, v_i)}. \tag{2.49}$$

If the degree of freedom is located at an edge between two cells, we choose the average of two single weighting functions defined on the adjecent cells e and e' according to

$$\boldsymbol{w}_i = \frac{1}{2}\delta^2(\boldsymbol{r} - \boldsymbol{r}_i) \left(\frac{1}{D^e}\boldsymbol{\xi}^e + \frac{1}{D^{e'}}\boldsymbol{\xi}^{e'} \right). \tag{2.50}$$

By choosing the weighting functions $\boldsymbol{w}_i$ according to the Petrov-Galerkin's scheme, the outer integral in the Eqs. (2.10) and (2.11) is reduced such that its integrand is evaluated at a single point.

2.5 Singular integrals

When the field point and the source point are sufficiently separated, Gaussian quadrature can be used directly for integration. However, the assembling procedure frequently involves field points that are located on the surface. This is known as the true-singularity case, since the integrand in the EFIE or MFIE equations becomes singular (weak or strong) due the Green's function.

Another case is when field points are located very close to the surface. In this case, the integrand becomes nearly singular (weak or strong) and this is referred to as the near-singularity case.

One technique for numerically evaluating integrands for these cases is to transform the integration domain so that the Jacobian of the transformation cancels the singularity produced by the factor $1/r^n$ of the Green's function. There exists many transformations in the literature that can handle singular (weak and strong) integrands on a triangle domain. However, most of these transformations handle planar triangles [19]. To integrate over curvilinear elements, as is the case in this thesis, a first-order Taylor expansion of the surface is constructed around the singularity. This tangential rectilinear domain may then be divided into triangular subdomains and, then, integrated with quadrature rules constructed for planar triangles.

2.5.1 Subdivision of the quadrilateral element

The mapping $\boldsymbol{r}(u, v)$, given by (2.22), describes the curved element S^{e} given the constraints $-1 \leq u \leq +1$ and $-1 \leq v \leq +1$. Although it is possible to evaluate the mapping outside the region $-1 \leq u \leq +1$ and $-1 \leq v \leq +1$, it should be avoided since it involves extrapolation based on higher-order polynomials, where the result often yields an extension of the curved surface that intersects with itself.

A method to alleviate this problem is to construct a first-order Taylor expansion of the surface, where the linearized surface is the tangent plane evaluated at the point $\boldsymbol{r}_0$, where $\boldsymbol{r}_0$ is the closest point on the surface to the fixed field point $\boldsymbol{r}_{\mathrm{f}}$. The linearization point $\boldsymbol{r}_0$ is determined by minimizing the cost function $g(u, v) = |\boldsymbol{r}(u, v) - \boldsymbol{r}_{\mathrm{f}}|^2$ subject to the constraints $-1 \leq u \leq +1$ and $-1 \leq v \leq +1$. By choosing this cost function, the derivatives $\frac{\partial g}{\partial u}$ and $\frac{\partial g}{\partial v}$ are continuous everywhere and a gradient-based solver may be exploited. The solution to the minimization problem is (u_0, v_0) and we have $\boldsymbol{r}_0 = \boldsymbol{r}(u_0, v_0)$.

The linearization $\boldsymbol{r}_{\mathrm{lin}}(u, v)$ of the curved surface is constructed from the covariant basis vectors $(\boldsymbol{a}_0, \boldsymbol{b}_0)$ evaluated at $\boldsymbol{r}_0$, which yields

$$\boldsymbol{r}_{\mathrm{lin}}(u, v) = \boldsymbol{r}_0 + \boldsymbol{a}_0(u - u_0) + \boldsymbol{b}_0(v - v_0). \tag{2.51}$$

In the following, we refer to $\boldsymbol{r}_{\mathrm{lin}}(u, v)$ as the *the linearized surface* that corresponds to the curved surface $\boldsymbol{r}(u, v)$, where no constraints are applied to u and v. Also, we introduce the *the linearized element* $\bar{S}^{\mathrm{e}}$ of the curved element S^{e}, where the linearized element $\bar{S}^{\mathrm{e}}$ is described by (2.51) subject to the constraints $-1 \leq u \leq +1$ and $-1 \leq v \leq +1$.

The linearized element $\bar{S}^{\mathrm{e}}$ is subdivided by constructing triangles based on the corner vertics of $\bar{S}^{\mathrm{e}}$ and the projected point $\boldsymbol{r}_{\mathrm{p}}$. The projection point $\boldsymbol{r}_{\mathrm{p}}$ is determined by minimizing the cost function $g_{\mathrm{lin}}(u, v) = |\boldsymbol{r}_{\mathrm{lin}}(u, v) - \boldsymbol{r}_{\mathrm{f}}|^2$ without any constraints on u and v. It is shown in Appendix B that the analytical solution to the minimization problem is found by solving the system of linear equations

$$\begin{bmatrix} |\boldsymbol{a}_0|^2 & \boldsymbol{a}_0 \cdot \boldsymbol{b}_0 \\ \boldsymbol{a}_0 \cdot \boldsymbol{b}_0 & |\boldsymbol{b}_0|^2 \end{bmatrix} \begin{bmatrix} u_{\mathrm{p}} \\ v_{\mathrm{p}} \end{bmatrix} = \begin{bmatrix} \boldsymbol{a}_0 \cdot (\boldsymbol{r}_{\mathrm{f}} - \boldsymbol{r}_0 + \boldsymbol{a}_0 u_0 + \boldsymbol{b}_0 v_0) \\ \boldsymbol{b}_0 \cdot (\boldsymbol{r}_{\mathrm{f}} - \boldsymbol{r}_0 + \boldsymbol{a}_0 u_0 + \boldsymbol{b}_0 v_0) \end{bmatrix}, \tag{2.52}$$

where $(u_{\mathrm{p}}, v_{\mathrm{p}})$ is the solution and we have $\boldsymbol{r}_{\mathrm{p}} = \boldsymbol{r}_{\mathrm{lin}}(u_{\mathrm{p}}, v_{\mathrm{p}})$. Four possible cases of the outcome of the subdivision are shown in Figures 2.6 - 2.9.

In practice, there are cases when $\boldsymbol{r}_{\mathrm{p}}$ is located very close to an edge or a corner of $\bar{S}^e$ such that extremely thin triangles are formed, where the height of the triangle is much shorter than its base and the area of the triangle is close to zero. These triangles are called *slivers* and the potential problem with slivers is discussed in later chapters.

2.5.2 Mapping to suitable domain for product integration rules

Thus, $\bar{S}^e$ is sub-divided into a set of sub-triangles and, possibly, sub-quadrilaterals. In the following, we consider a sub-triangle as a special case of a sub-quadrilateral.

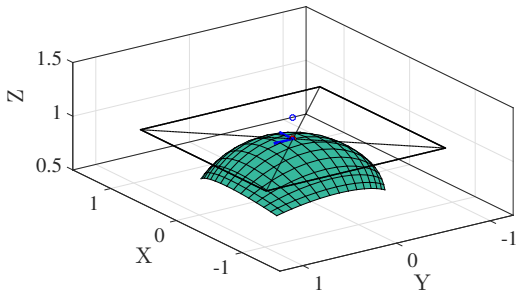

(a) Curved surface S^e and linearized surface $\bar{S}^e$.

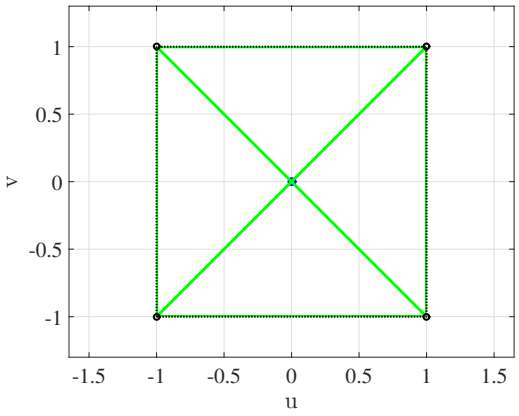

(b) Corresponding sub-division of triangles on the reference element.

Figure 2.6: Linearization point and projection point coincide inside the curved element. This yields $\boldsymbol{r}_0 = \boldsymbol{r}_\mathrm{p}$ with $-1 \leq u \leq +1$ and $-1 \leq v \leq +1$. We get four sub-triangles on $\bar{S}^e$.

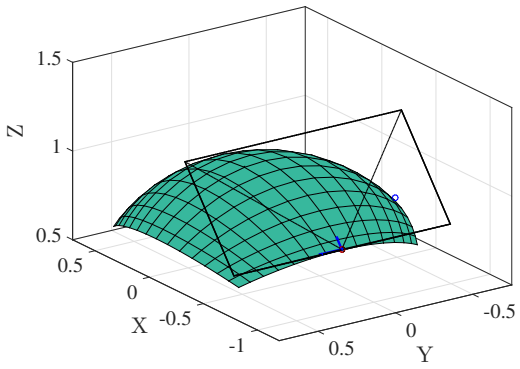

(a) Curved surface S^e and linearized surface $\bar{S}^e$.

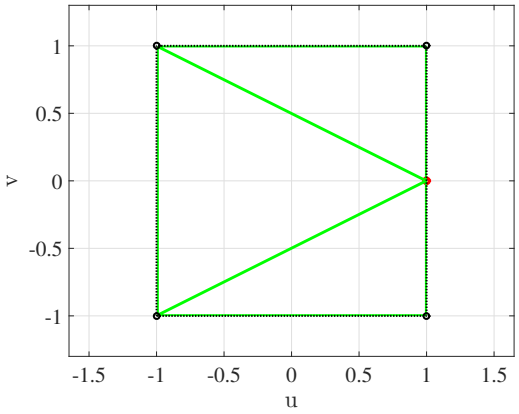

(b) Corresponding sub-division of triangles on the reference element.

Figure 2.7: Linearization point and projection point coincide on an edge of the curved element. This yields $\boldsymbol{r}_0 = \boldsymbol{r}_\mathrm{p}$ with $|u| = 1$ or $|v| = 1$, which corresponds to four special cases for the four edges. We get three sub-triangles on $\bar{S}^e$.

We refer these sub-elements as generalized quadrilaterals, where the triangle is featured as a special case.

A number of numerical integration schemes in the existing literature are formulated as a transformation from a triangle on $\bar{S}^e$ to a quadrilateral domain in a new coordinate system, which we refer to as the (p, q)-coordinate system below. It is feasible to extend such a numerical integration procedure in order to apply to the generalized quadrilaterals that we have given in the following observations:

- The projection point $\boldsymbol{r}_\mathrm{p}$ corresponds to $p = q = 0$. This implies that the singularity of the Green's function is most pronounced at the origin of the (p, q)-coordinate system and the objective is to find a quadrature scheme that efficiently deals with this singularity.

- The two (straight) edges of the generalized quadrilateral on $\bar{S}^e$ that coincide

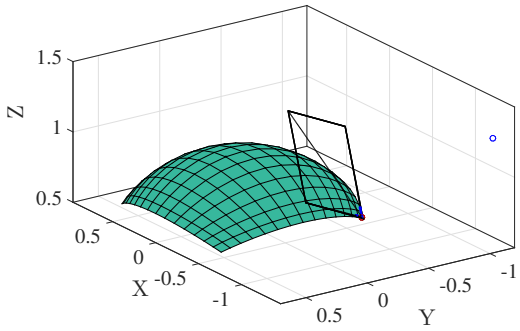

(a) Curved surface S^e and linearized surface $\bar{S}^e$.

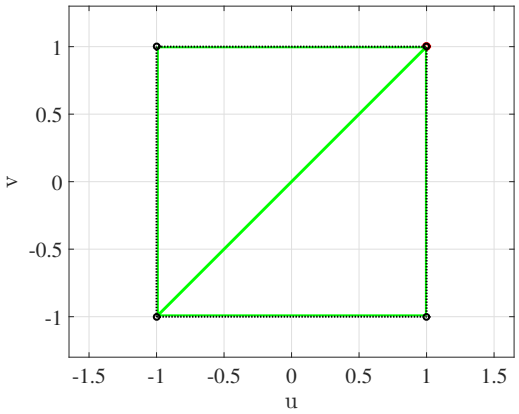

(b) Corresponding sub-division of triangles on the reference element.

Figure 2.8: Linearization point and projection point coincide on an corner of the curved element. This yields $\boldsymbol{r}_0 = \boldsymbol{r}_\mathrm{p}$ with $|u| = |v| = 1$, which corresponds to four special cases for the four corners. We get two sub-triangles on $\bar{S}^e$.

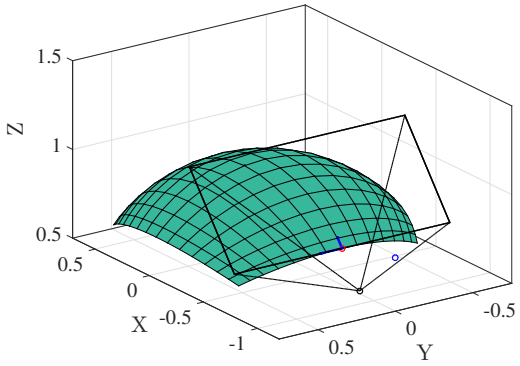

(a) Curved surface S^e and linearized surface $\bar{S}^e$.

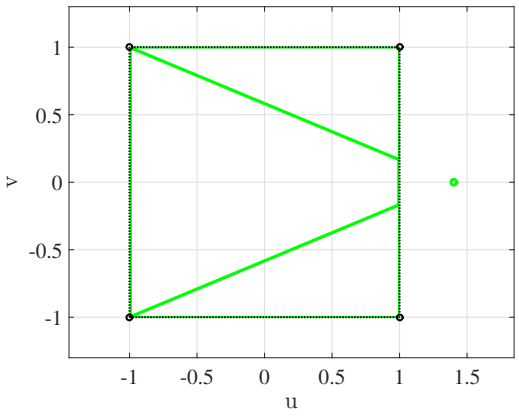

(b) Corresponding sub-division of triangles on the reference element.

Figure 2.9: Linearization point on an edge or at a corner of the curved element and the projection point is located elsewhere on the linearized surface. This yields $\boldsymbol{r}_0 \neq \boldsymbol{r}_\mathrm{p}$ with $|u| > 1$ and/or $|v| > 1$ for $\boldsymbol{r}_\mathrm{p}$, where the diagonals $|u| = |v|$ are excluded as this case is treated in Fig. 2.8. Notice that $\boldsymbol{r}_0$ is determined subject to the constraint $-1 \leq u \leq +1$ and $-1 \leq v \leq +1$ and, here, at least one of these constraints is active. In addition, we have a number of possible cases for the sub-division that may feature both triangles and quadrilaterals on $\bar{S}^e$.

with the two radial straight lines that intersect at $\boldsymbol{r}_\mathrm{p}$ are mapped to straight edges in the (p, q)-plane, where these straight edges can be described by a constant p-coordinate and $q > 0$. The two other straight edges of $\bar{S}^e$ map onto curves in the (p, q)-plane, where these curves may be expressed as functions $q = q_\mathrm{min}(p)$ and $q = q_\mathrm{max}(p)$. If the coordinates (p, q) are chosen to be the polar coordinates (ϕ, ρ), then a typical typical expression for these functions could be $\rho(\phi) = h/\sin\phi$, where h is the distance from the projection point to a line with constant u-coordinate in Figure 2.9(b) of the middle generalized quadrilateral with four sides and ϕ is the polar angle.

– A generalized quadrilateral that specializes to a triangle on the linearized element $\bar{S}^e$ may take different forms in the (p,q)-plane. Here, the collapsed edge of the generalized quadrilateral that corresponds to a point on $\bar{S}^e$ is transformed to a point in the (p,q)-plane.

Next, we construct quadrature schemes suitable for integration on the generalized quadrilaterals expressed in the (p,q)-plane.

– The integration limits $q_{\min}(p)$ and $q_{\max}(p)$ are generally piecewise functions with a discontinuous derivative at a small number of discrete points $p_1, p_2, \ldots, p_N$.

– We form a product rule for 2D by means of one-dimensional Gauss-quadrature schemes, where all quadrature points fall on lines of constant p.

– First, we integrate with respect to p along segments $p_i < p < p_{i+1}$ and, then, we integrate with respect to q from $q_{\min}(p)$ to $q_{\max}(p)$.

The quadrature weights and quadrature points are then mapped from the (p,q)-plane, via the linearized element $\bar{S}^e$ to the curved element S^e.

This procedure is illustrated in the following. Consider an integral of the form

$$I = \int_{S^e} h(\xi,\zeta)\,\mathrm{d}S, \tag{2.53}$$

where ξ and ζ are coordinates on the curved element S^e and $h(\xi,\zeta)$ represents the product of a basis function and the scalar Green's function. As described in Section 2.2.4, the intregral over S^e is transformed to the reference element according to $\mathrm{d}S = D(u,v)\mathrm{d}u\mathrm{d}v$. However, the integration could also be performed over the linearized element $\bar{S}^e$ according to $\mathrm{d}S_{\text{lin}} = D_0\mathrm{d}u\mathrm{d}v$, where $D_0 = |\boldsymbol{a}_0 \times \boldsymbol{b}_0|$ is computed at the point $\boldsymbol{r}_0$. This implies $\mathrm{d}S = \frac{D(u,v)}{D_0}\mathrm{d}S_{\text{lin}}$.

The linearized surface element $\bar{S}^e$ is then subdivided into generalized quadrilaterals and the integration over $\bar{S}^e$ is converted to a sum over all resulting generalized quadrilaterals Q, where the integration over each generalized quadrilateral is transformed to the (p,q)-coordinate system according to $\mathrm{d}S_{\text{lin}} = J_T\mathrm{d}q\mathrm{d}p$. Here, J_T is the Jacobian of the transformation rule, which cancels the singularity (weak or strong) in the Green's function. Hence, the integral (2.53) can finally be rewritten as

$$\int_{S^e} h(\xi,\zeta)\,\mathrm{d}S = \sum_{Q} \int_{p_{\min}}^{p_{\max}} \int_{q_{\min}(p)}^{q_{\max}(p)} h(u(p,q),v(p,q))\frac{D(u,v)}{D_0} J_T \mathrm{d}q\mathrm{d}p. \tag{2.54}$$

2.5.3 Integrands with weak singularity

The term that by immidiate inspection possess a weak singularity $(1/r)$ in the near-field representation of the operators (1.43) and (1.44) is

$$\int_S G(\boldsymbol{r},\boldsymbol{r}')\boldsymbol{X}(\boldsymbol{r}')\,\mathrm{d}S'. \tag{2.55}$$

It is shown in [20] that the tangential component of the $\mathcal{K}$-operator

$$\int_S \left([\nabla G(\boldsymbol{r},\boldsymbol{r}')] \times \boldsymbol{X}(\boldsymbol{r}')\right)_{tan}\mathrm{d}S', \tag{2.56}$$

also possess a weak singularity when the field point is located on the surface.

For integrands with a weak singularity, we exploit the Radial-Angular scheme [21] and apply it according to the procedure outlined in Section 2.5.2. This approach works for both the true and the near singularity.

2.5.4 Integrands with strong singularity

The terms that possess strong singularities ($1/r^2$) in the near-field representation of the operators (1.43) and (1.44) are

$$\int_S \nabla G(\boldsymbol{r}, \boldsymbol{r}') \nabla' \cdot \boldsymbol{X}(\boldsymbol{r}') \, \mathrm{d}S', \tag{2.57}$$

$$\int_S [\nabla G(\boldsymbol{r}, \boldsymbol{r}')] \times \boldsymbol{X}(\boldsymbol{r}') \, \mathrm{d}S', \tag{2.58}$$

where (2.58) contains a strong singularity for the near-singularity case.

True singularity

The integrand in (2.57) is the only term in the MoM formulation that possess a true strong singularity. A method first developed by Guiggiani [22] for handling true strong singularities in computational mechanics was reiterated by Weile [23] for computational electromagnetics. In this scheme, the integral is divided into parts that posses weak singularities and a part which is evaluated in the Cauchy principal value sense. The complete derivation can be found in Appendix C, below we just state the final results:

$$\begin{aligned} \int_S \nabla G(\boldsymbol{r}, \boldsymbol{r}') \nabla' \cdot \boldsymbol{X}(\boldsymbol{r}') \, \mathrm{d}S' = & \int_{\phi=0}^{2\pi} \int_{\rho=0}^{\beta(\phi)} \left[\boldsymbol{\Gamma}(\rho, \phi) - \frac{\boldsymbol{\gamma}(\phi)}{\rho} \right] \mathrm{d}\rho \mathrm{d}\phi \\ & + \int_{\phi=0}^{2\pi} \boldsymbol{\gamma}(\phi) \ln[\beta(\phi) P(\phi)] \mathrm{d}\rho \mathrm{d}\phi \\ & + \frac{\nabla \cdot \boldsymbol{X}(\boldsymbol{r})}{2} \hat{\boldsymbol{n}} \end{aligned} \tag{2.59}$$

The complete expressions for $\boldsymbol{\Gamma}$, $\boldsymbol{\gamma}$, P and β can be found in Appendix C.

Near singularity

For integrands with a near singularity, we exploit the scheme designed by Botha [11] and apply it according to the procedure outlined in 2.5.2.

Chapter 3

Results

A numerical MoM-solver is implemented in MATLAB and it is tested in three different settings: (i) scattered fields calculated from given source currents on a sphere; (ii) induced currents and far-field solution for a PEC scatterer given an incident plane wave; and (iii) induced currents and the near-field solution for two adjacent PEC spheres illuminated by a plane wave.

3.1 Integration of known surface current

In this section, the scattered fields from a given source current are analyzed. This serves as an intermediate test that verifies the expressions for the operators (1.37) and (1.38). The analytical expressions for the surface currents are derived from the multipole expansion, where a single mode is chosen for simplicity.

The MoM-formulation is tested by calculating the coefficients for each degree of freedom of the current expansion (2.41) given the currents

$$\boldsymbol{J}_s(\theta,\phi) = \hat{\boldsymbol{\theta}}\sqrt{\frac{3}{2\pi}}\frac{\mathbf{E}_0}{2Z_0}\frac{1+jka}{(ka)^2}e^{-jka}\sin(\theta), \tag{3.1}$$

$$\boldsymbol{M}_s(\theta,\phi) = \hat{\boldsymbol{\phi}}\sqrt{\frac{3}{2\pi}}\frac{\mathbf{E}_0}{ka}\left[\frac{1}{2}\left(kah_0^{(2)}(ka) - h_1^{(2)}(ka)\right)\sin(\theta)\right], \tag{3.2}$$

where a is the radius of the sphere, $\mathbf{E}_0$ is a complex amplitude and $h_1^{(2)}$, $h_0^{(2)}$ are spherical Hankel functions of second kind. The surface currents (3.1) and (3.2) produce scattered fields given by

$$\boldsymbol{E}(r,\theta,\phi) = \sqrt{\frac{3}{2\pi}}\frac{\mathbf{E}_0}{kr}\left[\hat{\boldsymbol{r}}h_1^{(2)}(kr)\cos(\theta) + \hat{\boldsymbol{\theta}}\frac{1}{2}\left(h_1^{(2)}(kr) - krh_0^{(2)}(kr)\right)\sin(\theta)\right], \tag{3.3}$$

$$\boldsymbol{H}(r,\theta,\phi) = -\hat{\boldsymbol{\phi}}\sqrt{\frac{3}{2\pi}}\frac{\mathbf{E}_0}{2Z_0}\frac{1+jkr}{(kr)^2}e^{-jkr}\sin(\theta). \tag{3.4}$$

The expressions for the analytical surface currents and fields are derived in Appendix D.

Given the surface currents, the scattered fields may be computed from the numerical expressions for the current expanded in the known coefficients and basis functions. The coefficients are computed from

$$\int_S \boldsymbol{w}_i \cdot \boldsymbol{X}_{\mathrm{a}}(\boldsymbol{r})\,\mathrm{d}S = \int_S \boldsymbol{w}_i \cdot \boldsymbol{X}_{\mathrm{n}}(\boldsymbol{r})\,\mathrm{d}S, \tag{3.5}$$

where $\boldsymbol{X}_{\mathrm{a}}$ is the analytical expression for the current and $\boldsymbol{X}_{\mathrm{n}}$ is the numerical expression for the current given by (2.41). Equation (3.5) is solved for the weighting function (2.46) and the expression for the basis functions (2.41), which yields

$$X^U_{ij,e} = (\boldsymbol{a} \cdot \boldsymbol{X}) \det \mathbf{J}^e, \tag{3.6}$$

$$X^V_{ij,e} = (\boldsymbol{b} \cdot \boldsymbol{X}) \det \mathbf{J}^e, \tag{3.7}$$

where $\boldsymbol{X}$ is the analytical surface current $\boldsymbol{J}$ or $\boldsymbol{M}$, $\boldsymbol{a}$ and $\boldsymbol{b}$ are the covariant basis vectors.

3.1.1 Error analysis

In this section, the error of the MoM-formulation is analyzed, given a known source current. The electric and magnetic field are computed by Eqs. (1.37), (1.38) and compared to the analytical expressions (3.3) and (3.4). The absolute and the relative error for a vector field $\boldsymbol{F}$ can be calculated according to

$$\text{Absolute Error} = |\boldsymbol{F}_{\mathrm{num}} - \boldsymbol{F}_{\mathrm{ana}}|, \tag{3.8}$$

$$\text{Relative Error} = \frac{|\boldsymbol{F}_{\mathrm{num}} - \boldsymbol{F}_{\mathrm{ana}}|}{|\boldsymbol{F}_{\mathrm{ana}}|}, \tag{3.9}$$

where $\boldsymbol{F}_{\mathrm{num}}$ is the numerically computed result and $\boldsymbol{F}_{\mathrm{ana}}$ is the analytical field. We asssume that total error e_{tot} can be expressed as

$$e_{\mathrm{tot}} = e_{\mathrm{map}} + e_{\mathrm{vec}} + e_{\mathrm{int}}, \tag{3.10}$$

where e_{map} is the error associated with the mapping of the geometry, e_{vec} is the error associated with the discretization of the current and e_{int} is the error that stems from the integration scheme.

In the following tests, the error of the $\boldsymbol{E}$-field and $\boldsymbol{H}$-field are analyzed by varying one of the spatial coordinates. The radius of the sphere is set to $a = 1\mathrm{m}$, the frequency is set by the ratio $a/\lambda = 0.1$, the order of the mapping and integration scheme fixed to 12 and the order of the current discretization set to $p = 2,\ 4,\ 6$. The sphere is discretized with six curvilinear quadrilateral cells. Thus, we expect that e_{vec} is significantly larger than e_{map} and e_{int}.

For direct Gaussian quadrature, we compute the fields as a function of the field point as it approaches the surface of the sphere. Here, the dyadic Green's functions (1.63) and (1.64) are used for the $\mathcal{L}$ and $\mathcal{K}$ operators. The relative and absolute errors for the fields $\boldsymbol{E}$ and $\boldsymbol{H}$ are calculated with (3.9) and (3.8), where the results are shown in Fig. 3.1.

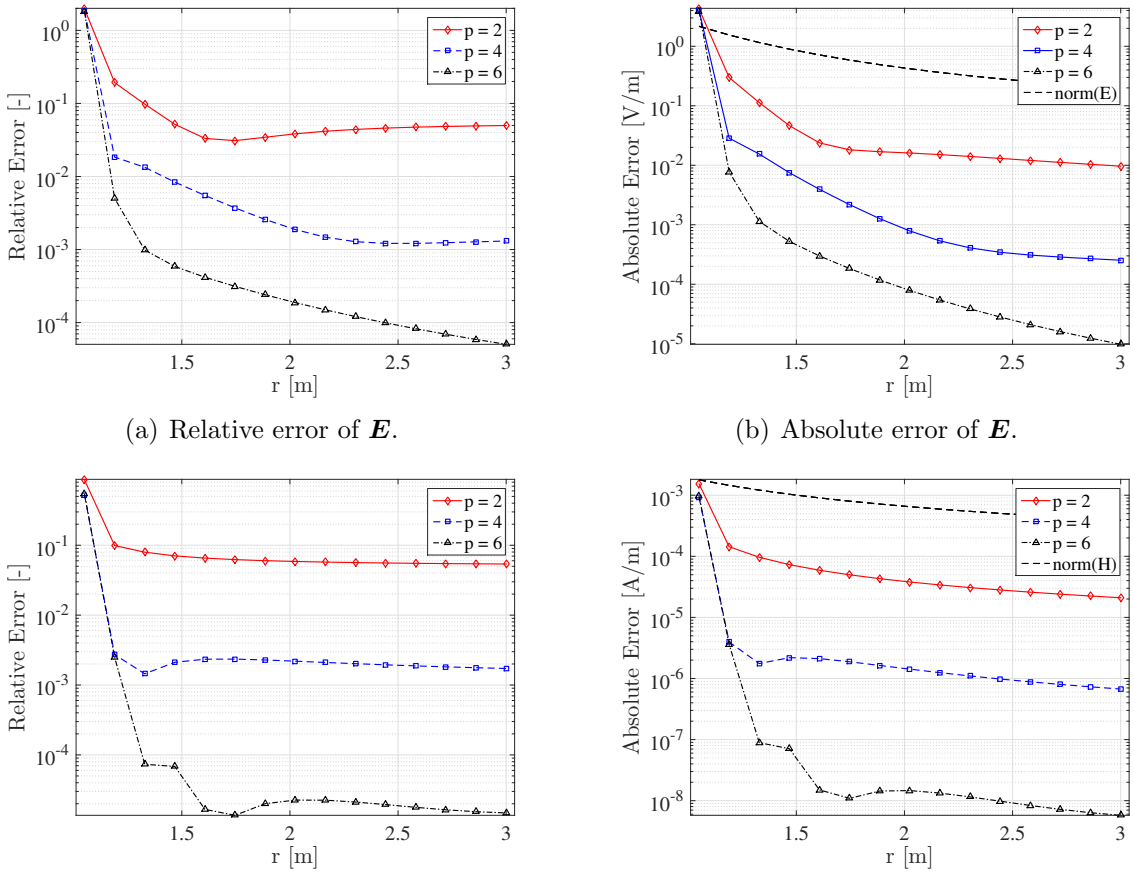

(a) Relative error of $\boldsymbol{E}$.

(b) Absolute error of $\boldsymbol{E}$.

(c) Relative error of $\boldsymbol{H}$.

(d) Absolute error of $\boldsymbol{H}$.

Figure 3.1: Errors of $\boldsymbol{E}$ and $\boldsymbol{H}$ by varying the distance of the field point in the direction $\theta = 45°$, $\phi = 45°$; solid curve - $p = 2$; dashed curve - $p = 4$; and dashed-dotted curve - $p = 6$.

The errors increase as the field point moves towards the surface of the sphere. For sufficiently small distance, direct Gaussian quadrature yields large errors due to the $1/r$ dependence of the Green's function. We also conclude that the error decreases for higher order of p.

Next, the angular dependence of the error is analyzed, i.e. the field point is varied at a fixed distance $3a$ around the sphere. The remaining paramters that describe the problem are fixed to the same values that are used in Fig. 3.1. The relative mean square angular error is computed by

$$\text{Relative Error} = \left[\frac{1}{4\pi}\oint_{S_\Omega}\frac{|\boldsymbol{F}_{num}-\boldsymbol{F}_{ana}|^2}{|\boldsymbol{F}_{ana}|^2}\mathrm{d}\Omega\right]^{\frac{1}{2}}, \tag{3.11}$$

where $\mathrm{d}\Omega$ is the solid angle and the fields are sampled at a distance $r = 3a$. The integral (3.11) is evaluated with 12-th order Gaussian quadrature scheme in both θ- and ϕ-direction. The result is shown in Fig. 3.2.

The graphs for $\boldsymbol{E}$ and $\boldsymbol{H}$ are nearly indistinguishable. A linear decrease of the error in the above semi-log graph indicates an exponential convergence of the error as p is increased.

Finally, the error is analyzed as a function of the frequency. The remaining

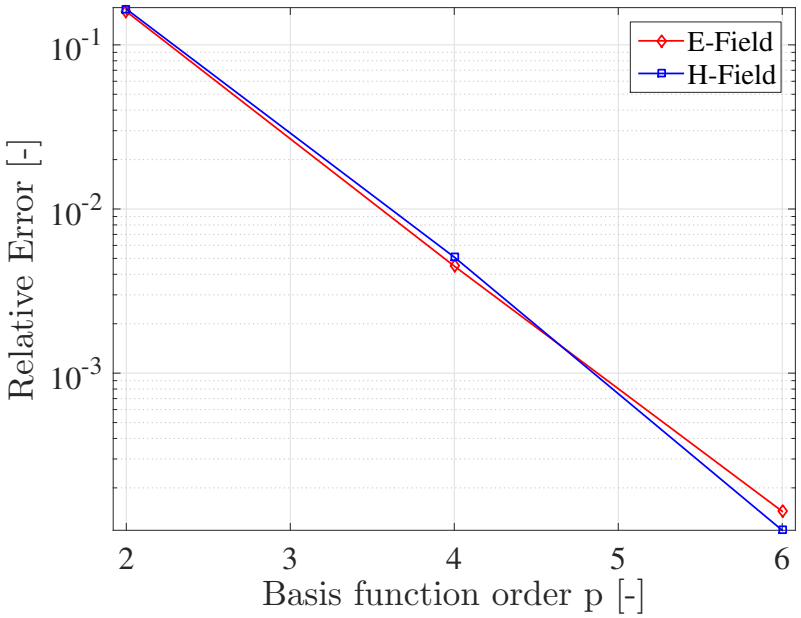

Figure 3.2: Plot showing the mean square angular error for $\boldsymbol{E}$ and $\boldsymbol{H}$.

paramters that describe the problem are fixed to the same values that are used in Fig. 3.1. However, the field point is fixed to a distance $3a$ from the origin. The frequency is varied such that $a/\lambda \in [10^{-4}, 10^{2}]$ and the results are shown in Fig. 3.3.

For wavelengths $\lambda > 100a$, the problem tends to an electrostatic problem. Thus, the error increases for the magnetic field for $\lambda > 100a$, whereas the error stays constant for the electric field. For shorter wavelenghts, the error increases for both the electric and magnetic field and the relative error is rather large for $\lambda < a$.

3.2 Scattering from PEC sphere

In this section, the MoM-formulation is tested for a PEC sphere of finite radius a. The excitation source is assumed to be an incoming plane wave, where the electric field given by Eq. (2.19). We set the propagation direction to $\hat{\boldsymbol{k}} = -\hat{\boldsymbol{z}}$ and the polarization to $\mathbf{E}_0 = \hat{\boldsymbol{x}}\mathbb{E}_0$ with unit amplitude $\mathbb{E}_0 = 1$. Given the incoming field, the EFIE for the impedance matrix (2.13) and the excitation vector (2.15) are computed. Next, the electric surface current is determined by solving the system of linear equations (2.12). With the coefficients of the induced current known, the scattered electric field is calculated with (1.37). In this case, the exact value for the scattered electric far-field may be expressed as a Mie-series expansion [25] for comparison. A quantity of interest is the radar cross section (RCS), which is defined as [7]

$$\sigma = 4\pi r^2 \frac{|\boldsymbol{E}^{\mathrm{s}}|^2}{|\boldsymbol{E}^{\mathrm{i}}|^2}, \tag{3.12}$$

where the scattered field $\boldsymbol{E}^{\mathrm{s}}$ is computed in the far-field region. The bistatic RCS is computed in the $\phi = 0°$ plane and compared to the Mie-series expansion for a frequency corresponding to $a/\lambda = 0.1$. The sphere is discretized with 24 curvilinear quadrilateral cells. The RCS as a function of θ is plotted in Fig. 3.4. The EFIE

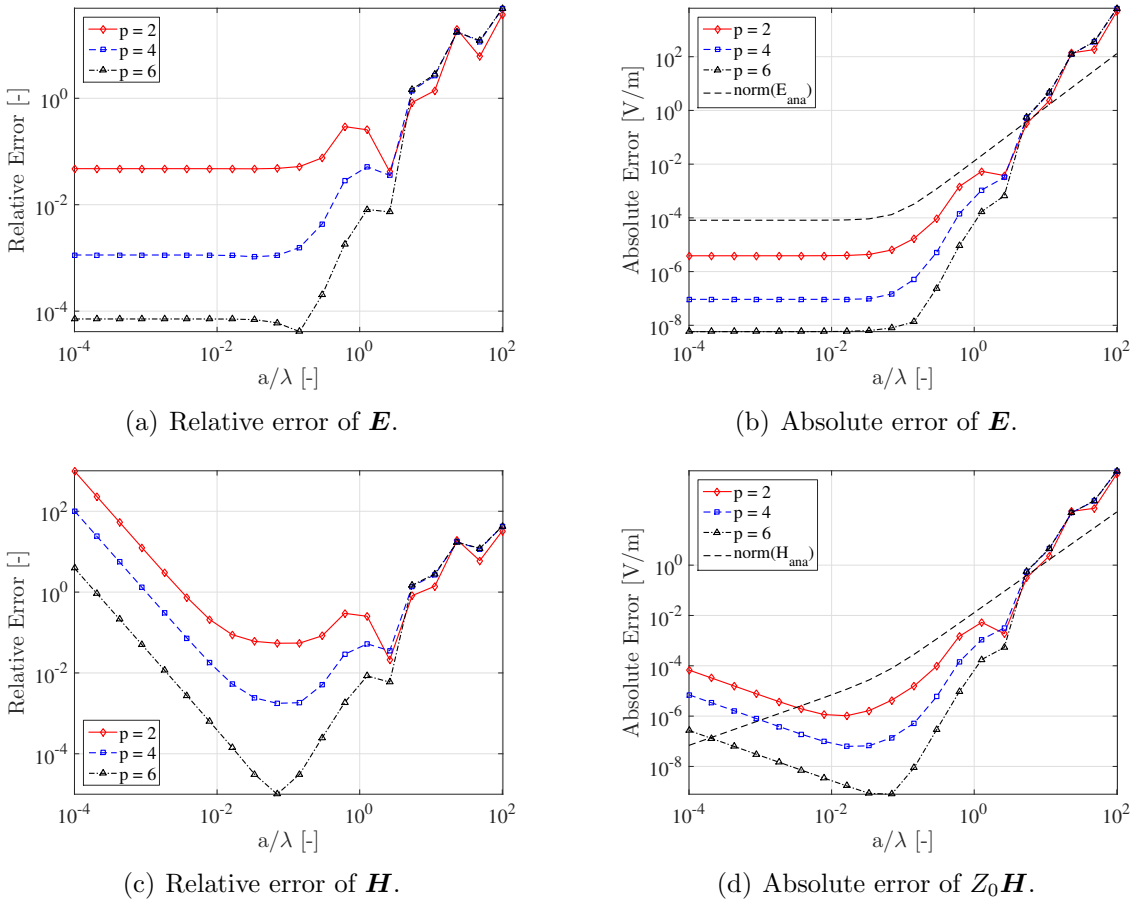

(a) Relative error of $\boldsymbol{E}$.

(b) Absolute error of $\boldsymbol{E}$.

(c) Relative error of $\boldsymbol{H}$.

(d) Absolute error of $Z_0\boldsymbol{H}$.

Figure 3.3: Errors of $\boldsymbol{E}$ and $\boldsymbol{H}$ as a function of the normalized frequency. The distance of the field point is fixed to $r = 3a$ in the direction $\theta = 45°$, $\phi = 45°$; solid curve - $p = 2$; dashed curve - $p = 4$; and dashed-dotted curve - $p = 6$.

result agrees very well with the Mie-series expansion, even for low-order vector basis functions. The root-mean-square error (RMSE) of the RCS can be calculated with

$$\text{RMSE} = \left[\frac{1}{N_\theta} \sum_{i=1}^{N_\theta} \frac{|\sigma^{\text{EFIE}}(\theta_i) - \sigma^{\text{Mie}}(\theta_i)|^2}{|\sigma^{\text{Mie}}(\theta_i)|^2} \right]^{\frac{1}{2}}, \tag{3.13}$$

where N_θ is the number of point sampled in θ. The RMSE as function of vector basis order is plotted in Fig. 3.5. Again, we note that the error decreases exponentially with the order p of the divergence-conforming basis functions. Moreover, the bistatic error is analyzed as a function of cell size h. The order of convergence in the cell size h_i (for $i = 0,\ 1,\ 2$) is estimated through carrying out computations for a geometric sequence of cell sizes such that $h_i/h_{i+1} = h_{i+1}/h_{i+2}$. We use cell sizes h_i that correspond to discretizing the surface of the sphere with 6, 24 and 96 curvelinear quadrilateral elements. The bistatic error is calculated from Eq. (3.11) and the result is shown in Fig. 3.6. For orders $p = 2$ and 4, the results form straight lines in the log-log plot, with a steeper slope for the latter case. For the order $p = 6$, the error increases unexpectedly from $h_i/h_0 = 0.5$ to $h_i/h_0 = 0.25$. The leading error

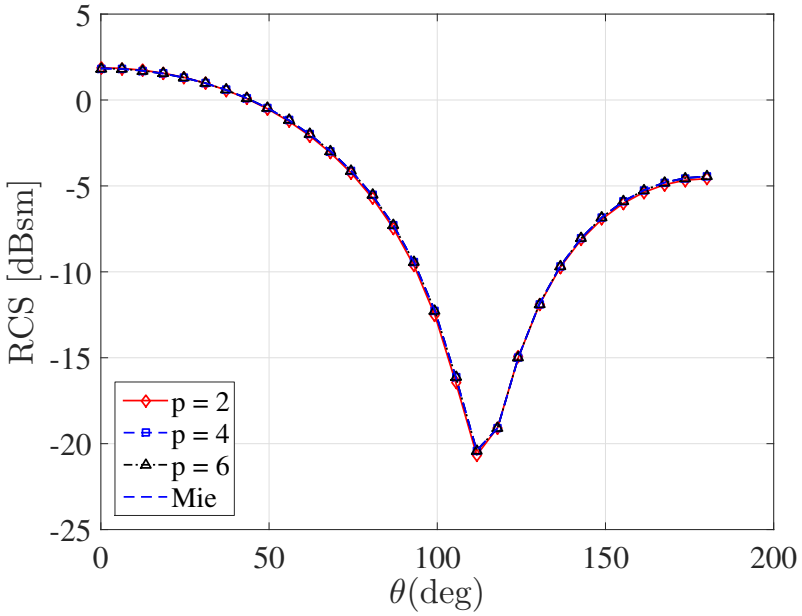

Figure 3.4: RCS as a function of θ for $a/\lambda = 0.1$.

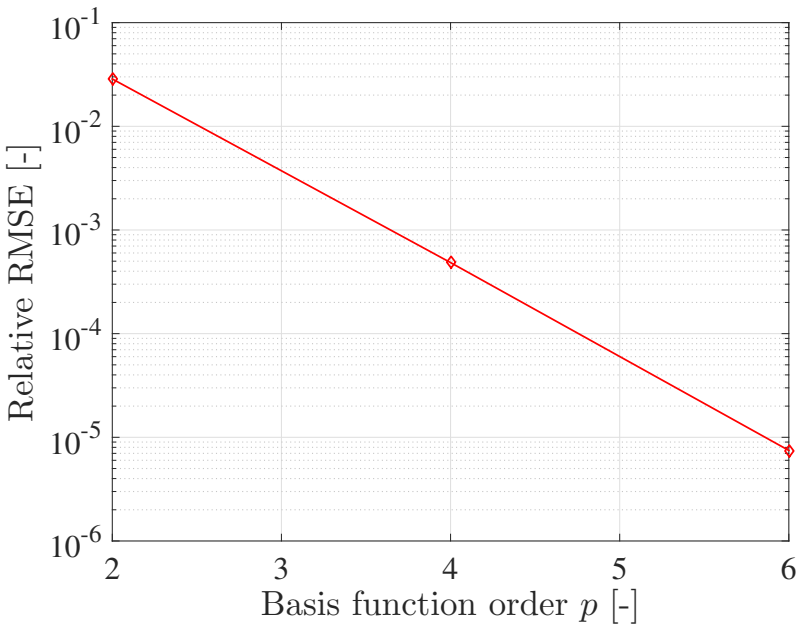

Figure 3.5: RMSE in the RCS of the EFIE solution for $a/\lambda = 0.1$.

can be assumed to be the lowest-order term in the series expansion of the error [8]

$$I(h) \approx I_0 + I_\alpha h^\alpha. \tag{3.14}$$

where I_0 is the extrapolated result and α is the order of convergence. For cell sizes that form a geometric series, it is possible to estimate the order of convergence [8] by

$$\alpha = \ln\left[\frac{I(h_i) - I(h_{i+1})}{I(h_{i+1}) - I(h_{i+2})}\right] / \ln\left[\frac{h_i}{h_{i+1}}\right]. \tag{3.15}$$

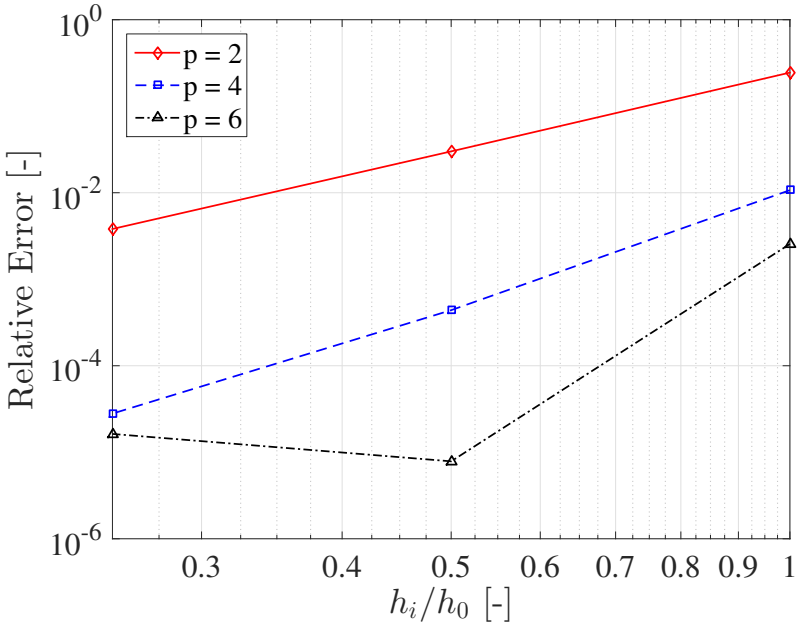

Figure 3.6: Bistatic error of the EFIE solution as a function of the normalized cell size h for $a/\lambda = 0.1$; solid curve - $p = 2$; dashed curve - $p = 4$; and dashed-dotted curve - $p = 6$.

When applied to the computed result in Fig. 3.6 for $h_i/h_0 = 1,\ 0.5,$ and 0.25, this formula gives $\alpha = 3.0318$ for $p = 2$ and $\alpha = 4.6429$ for $p = 4$. For $p = 6$ it is not possible to get a realiable order of convergence from the numerical result. The leading error is expected to scale as $\alpha = 2p$. By inspection of the result for the cases $p = 2$ and 4, it is noted that the resulting order of convergence is approximately a factor of 0.75 and 0.56, respectively, of the theoretical value $\alpha = 2p$.

3.3 Scattering from two PEC spheres

In this section, the MoM-formulation is tested on two adjacent PEC spheres, where both sphere have the radius a. The centers of the spheres are separated by $2.5a$ and they are illuminated by a plane wave with a frequency that corresponds to $a/\lambda = 0.1$, where $\mathbf{E}_0 = 1$. The near-field around the spheres is calculated for (i) horizontal polarization - an incoming electric field polarized along the straight line between the centers of the spheres and (ii) vertical polarization - an incoming field polarized perpendicular to the straight line between the centers of the spheres.

Figure 3.7 shows the electric field in the plane $z = 0$ for an incident electric field with polarization along the straight line between the center of the sphere, i.e. horizontal polarization as described above. In Fig. 3.7, it is possible to see an enhanced field with roughly 2.5 times the amplitude of the incoming field between the spheres.

Figure 3.8 shows the corresponding field plot for the incoming electric field vertically polarized as described in (ii) above. The enhanced field between the spheres does not occur for this polarization. Here, the maximum amplitude of the scattered near-field is only a factor 1.6 times the amplitude of the incoming field, thus, it is possible to conclude that the interaction between the spheres is stronger for the

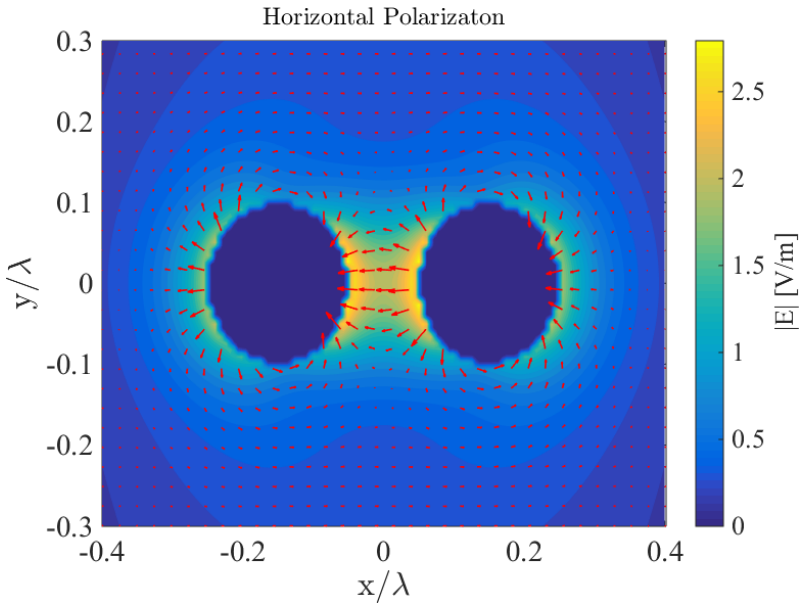

Figure 3.7: The electric field around the spheres for $a/\lambda = 0.1$. The background color represents the magnitude of the field and the red vector field the direction of the field.

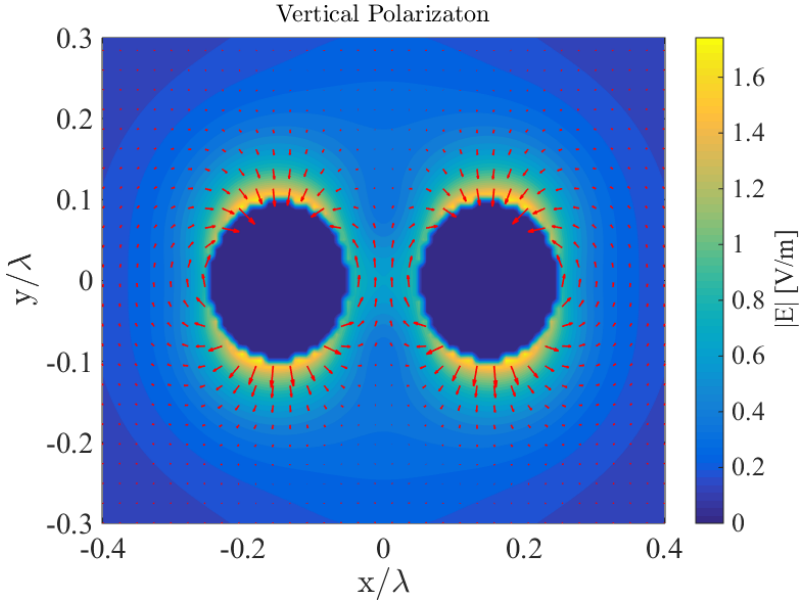

Figure 3.8: The electric field around the spheres for $a/\lambda = 0.1$. The background color represents the magnitude of the field and the red vector field the direction of the field.

horizontal polarization described in (i).

Chapter 4

Conclusions and future work

This thesis presents a Method of Moments (MoM) that exploits collocation in combination with higher-order interpolatory divergence-conforming basis functions for Maxwell's equations. In this chapter, the main findings of the work are presented together with some suggestions for future work.

4.1 Conclusions

The main focus is to investigate scattering problems treated by higer-order MoM. The differential Maxwell's equations are reformulated as the electric field integral equations by introducing a Green's function. The electric field integral equation (EFIE) is reduced to a computational domian that only involves the surface of the scatterer.

The MoM formulation is derived by the weighted residual method applied to the EFIE. We exploit a collocation scheme for testing the EFIE, which could effectively reduce the computational work required to evaluate the integrals in the EFIE formulation.

The geometry is discretized by high-order curvelinear quadrilateral cells, where Lagrangian polynomials are chosen for interpolation. An equal area mapping is used to discretize the surface of the sphere into cells of uniform size.

The currents are expanded divergence-conforming basis functions, with interpolatory nodes that are collocated with the underlying quadrature schemes. This reduces the integration for any given order to a single evaluation of the integrand at the interpolatory node.

The singular integrals in the resulting EFIE formulation could effectively be treated by subdividing the quadrilateral cell into triangles, where it is possible to cancel the singularity with well-chosen coordinate transformations. However, triangles resulting in slivers are hard to treat accurately with numerical integration and they may produce errors that are large. Singularity extraction is used for strong singularities.

The results show that the computer implemention of the MoM formulation could effectively reproduce analytical results for PECs. The MoM formulation is showed to converge exponentially with increasing vector basis order p. However, the current computer implementation could not reproduce a leading error proportional to h^{2p},

where h is the cell size.

4.2 Future work

The topics covered in this work could be applied on many interesting problems. The applicability of this work could be extended by including the modeling of dielectric objects. For example, the field of plasmons is connected to internal oscillations of electrons inside a metal. This corresponds to the presence of electric fields inside the metal and the PEC approximation can not deal with those cases. A natural continuation of this work would then be to include modeling of dielectrics.

Bibliography

[1] H. Jiang, L. Xu, and K. Zhan, "Joint tracking and classification based on aerodynamic model and radar cross section," *Pattern Recognition*, vol. 47, no. 9, pp. 3096–3105, 2014.

[2] O. I. Sukharevsky, "Electromagnetic Wave Scattering by Aerial and Ground Radar Objects," no. 2, pp. 162–167, 2015.

[3] L. Ying, W. Zhe, H. Peilin, and L. Zhanhe, "A New Method for Analyzing Integrated Stealth Ability of Penetration Aircraft," *Chinese Journal of Aeronautics*, vol. 23, no. 2, pp. 187–193, 2010.

[4] Y. Li, J. Huang, S. Hong, Z. Wu, and Z. Liu, "A new assessment method for the comprehensive stealth performance of penetration aircrafts," *Aerospace Science and Technology*, vol. 15, no. 7, pp. 511–518, 2011.

[5] H. Garcia, R. Sachan, and R. Kalyanaraman, "Optical Plasmon Properties of Co-Ag Nanocomposites Within the Mean-Field Approximation," *Plasmonics*, vol. 7, no. 1, pp. 137–141, 2012.

[6] D. Albinsson, "Complex plasmonic nanostructures for materials science and catalysis," 2015. 64.

[7] J. D. Jackson, "Classical Electrodynamics," 1999.

[8] A. Bondeson, T. Rylander, and P. Ingelström, *Computational Electromagnetics*. External organization, 2005. 222.

[9] W. Gibson, *The Method of Moments in Electromagnetics*. No. 2, 2007.

[10] P. W. Fink, D. R. Wilton, and M. a. Khayat, "Simple and Efficient Numerical Evaluation of Near-Hypersingular Integrals," *Antennas and Wireless Propagation Letters, IEEE*, vol. 7, pp. 469–472, 2008.

[11] M. M. Botha, "Numerical Integration Scheme for the Near-Singular Green Function Gradient on General Triangles," *IEEE Transactions on Antennas and Propagation*, vol. 63, no. 10, pp. 4435–4445, 2015.

[12] G. B. Arfken, *Mathematical Methods for Physicists, 4th ed.*, vol. 67. 1999.

[13] R. F. Boisvert and D. W. Lozier, "Handbook of Mathematical Functions," *A Century of Excellence in Measurements, Standards, and Technology - A Chronicle of Selected NBS/NIST Publications, 1901-2000*, pp. 135–139, 2001.

[14] D. Roşca and G. Plonka, "Uniform spherical grids via equal area projection from the cube to the sphere," *Journal of Computational and Applied Mathematics*, vol. 236, no. 6, pp. 1033–1041, 2011.

[15] A. F. Peterson, *Mapped Vector Basis Functions for Electromagnetic Integral Equations*, vol. 1. 2006.

[16] F. B. Hildebrand, *Introduction to numerical analysis*. 1987.

[17] A. Quarteroni, R. Sacco, F. Saleri, *Numerical Mathematics*. 2007.

[18] S. Rao, D. Wilton, and a. Glisson, "Electromagnetic scattering by surfaces of arbitrary shape," *IEEE Transactions on Antennas and Propagation*, vol. 30, no. 3, pp. 409–418, 1982.

[19] D. R. Wilton, F. Vipiana, and W. a. Johnson, "Evaluating Singular, Near-Singular, and Non-Singular Integrals on Curvilinear Elements," *Electromagnetics*, vol. 34, no. 3-4, pp. 307–327, 2014.

[20] S. D. Gedney, "On Deriving a Locally Corrected Nyström Scheme from a Quadrature Sampled Moment Method," *IEEE Transactions on Antennas and Propagation*, vol. 51, no. 9, pp. 2402–2412, 2003.

[21] M. a. Khayat and D. R. Wilton, "Numerical evaluation of singular and near-singular potential integrals," *IEEE Transactions on Antennas and Propagation*, vol. 53, no. 10, pp. 3180–3190, 2005.

[22] M. Guiggiani and a. Gigante, "A General Algorithm for Multidimensional Cauchy Principal Value Integrals in the Boundary Element Method," *Journal of Applied Mechanics*, vol. 57, no. 4, p. 906, 1990.

[23] D. S. Weile and X. Wang, "Strong singularity reduction for curved patches for the integral equations of electromagnetics," *IEEE Antennas and Wireless Propagation Letters*, vol. 8, no. 2, pp. 1370–1373, 2009.

[24] Michael G. Duffy, "Quadrature Over a Pyramid or Cube of Integrands with a Singularity at a Vertex," *SIAM Journal on Numerical Analysis*, vol. 19, no. 6, pp. 1260–1262, 1982.

[25] C. a. Balanis, *Advanced Engineering Electromagnetics*, vol. 52. 1989.

Appendix A

Far-field derivation for $\mathcal{L}$ and $\mathcal{K}$

In this section, we want to find the far-field expressions for the operators

$$(\mathcal{L}\boldsymbol{X})(\boldsymbol{r}) = \left[1 + \frac{1}{k^2}\nabla\nabla\cdot\right]\int_S G(\boldsymbol{r},\boldsymbol{r}')\boldsymbol{X}(\boldsymbol{r}')\,\mathrm{d}S', \tag{A.1}$$

$$(\mathcal{K}\boldsymbol{X})(\boldsymbol{r}) = \nabla\times\int_S G(\boldsymbol{r},\boldsymbol{r}')\boldsymbol{X}(\boldsymbol{r}')\,\mathrm{d}S's, \tag{A.2}$$

given the 3D, homogeneous, scalar Green's function

$$G(\boldsymbol{r},\boldsymbol{r}') = \frac{e^{-jk|\boldsymbol{r}-\boldsymbol{r}'|}}{4\pi|\boldsymbol{r}-\boldsymbol{r}'|}. \tag{A.3}$$

We start with the expression for $\mathcal{L}$. We rewrite the distance $|\boldsymbol{r}-\boldsymbol{r}'|$ between the source point $\boldsymbol{r}'$ and observation point $\boldsymbol{r}$ as a scalar product

$$|\boldsymbol{r}-\boldsymbol{r}'| = \sqrt{(\boldsymbol{r}-\boldsymbol{r}')\cdot(\boldsymbol{r}-\boldsymbol{r}')} = \sqrt{r^2 - r'^2 - 2\boldsymbol{r}\cdot\boldsymbol{r}'}$$

where $r = |\boldsymbol{r}|$ and $r' = |\boldsymbol{r}'|$. We can approximate the leading contribution from this distance as

$$\begin{aligned}|\boldsymbol{r}-\boldsymbol{r}'| &= r\sqrt{1 + (\frac{r'}{r})^2 - 2\hat{\boldsymbol{r}}\cdot\frac{\boldsymbol{r}'}{r}} = r\left\{1 + \frac{1}{2}\left[\left(\frac{r'}{r}\right)^2 - 2\hat{\boldsymbol{r}}\cdot\frac{\boldsymbol{r}'}{r}\right] + \ldots\right\} \\ &= r - \hat{\boldsymbol{r}}\cdot\boldsymbol{r}' + \mathcal{O}(d^2/r), \text{as} \to \infty,\end{aligned} \tag{A.4}$$

where we have used $\sqrt{1+x} = 1 + x/2 + \ldots$ and defined

$$d = \max|\boldsymbol{r}'|$$

as the maximum extension of the scatterer. The Green's function may then be rewritten as

$$\begin{aligned}G(\boldsymbol{r},\boldsymbol{r}') = \frac{e^{-jk|\boldsymbol{r}-\boldsymbol{r}'|}}{4\pi|\boldsymbol{r}-\boldsymbol{r}'|} &= \frac{\exp(-jk(r - \hat{\boldsymbol{r}}\cdot\boldsymbol{r}' + \mathcal{O}(d^2/r))}{4\pi r(1+\mathcal{O}(d/r))} \\ &= \frac{e^{-jkr}}{4\pi r}e^{-jk\hat{\boldsymbol{r}}\cdot\boldsymbol{r}'}(1+\mathcal{O}(kd^2/r))(1+\mathcal{O}(d/r)).\end{aligned}$$

The leading contribution from (A.1) becomes then

$$(\mathcal{L}\boldsymbol{X})(\boldsymbol{r}) = \left[1 + \frac{1}{k^2}\nabla\nabla\cdot\right]\frac{e^{-jkr}}{kr}\frac{k}{4\pi}\int_S e^{-jk\hat{\boldsymbol{r}}\cdot\boldsymbol{r}'}\boldsymbol{X}(\boldsymbol{r}')\,\mathrm{d}S', \tag{A.5}$$

where we have used $r \gg d$ and $r \gg kd^2$. It is convenient to define

$$\boldsymbol{P}(\hat{\boldsymbol{r}}) = \frac{k}{4\pi}\int_S e^{-jk\hat{\boldsymbol{r}}\cdot\hat{\boldsymbol{k}}}\boldsymbol{X}(\boldsymbol{r}')\,\mathrm{d}S', \tag{A.6}$$

where $\boldsymbol{P}$ is essentially the spatial Fourier transform of the current density $\boldsymbol{X}$ evaluated in the point $k\hat{\boldsymbol{r}}$. Equation (A.5) can then be rewritten as

$$(\mathcal{L}\boldsymbol{X})(\boldsymbol{r}) = \left[1 + \frac{1}{k^2}\nabla\nabla\cdot\right]\left(\frac{e^{-jkr}}{kr}\boldsymbol{P}(\hat{\boldsymbol{r}})\right).$$

Evaluating the contribution from divergence operator gives

$$\nabla\cdot\left(\frac{e^{-jkr}}{kr}\boldsymbol{P}(\hat{\boldsymbol{r}})\right) = \frac{e^{-jkr}}{kr}\nabla\cdot\boldsymbol{P}(\hat{\boldsymbol{r}}) + \boldsymbol{P}(\hat{\boldsymbol{r}})\cdot\nabla\left(\frac{e^{-jkr}}{kr}\right).$$

Since $\boldsymbol{P}(\hat{\boldsymbol{r}}) = \boldsymbol{P}(\phi,\theta)$, we get in spherical coordinates

$$\begin{aligned}\nabla\cdot\boldsymbol{P}(\hat{\boldsymbol{r}}) &= \frac{1}{r\sin\theta}\frac{\partial(\sin\theta P_\theta)}{\partial\theta} + \frac{1}{r\sin\theta}\frac{\partial P_\phi}{\partial\phi} \propto \frac{1}{r},\\ \nabla\left(\frac{e^{-jkr}}{kr}\right) &= \hat{\boldsymbol{r}}(-jk - \frac{1}{r})\frac{e^{-jkr}}{kr}.\end{aligned}$$

This gives

$$\begin{aligned}\frac{1}{k}\nabla\cdot\left[\frac{e^{-jkr}}{kr}\boldsymbol{P}(\hat{\boldsymbol{r}})\right] &= \frac{e^{-jkr}}{(kr)^2}\frac{1}{\sin\theta}\left[\frac{\partial(\sin\theta P_\theta)}{\partial\theta} + \frac{\partial P_\phi}{\partial\phi}\right]\\ &\quad + \boldsymbol{P}(\hat{\boldsymbol{r}})\cdot\hat{\boldsymbol{r}}(-jk - \frac{1}{r})\frac{e^{-jkr}}{kr}\\ &= -j\boldsymbol{P}(\hat{\boldsymbol{r}})\frac{e^{-jkr}}{kr}(1 + \mathcal{O}((kr)^{-1})).\end{aligned}$$

Similary, we get

$$\begin{aligned}\frac{1}{k}\nabla\left[\frac{1}{k}\nabla\cdot\left(\frac{e^{-jkr}}{kr}\boldsymbol{P}(\hat{\boldsymbol{r}})\right)\right] &= \frac{1}{k}\hat{\boldsymbol{r}}\frac{\partial}{\partial r}\left[-j\hat{\boldsymbol{r}}\cdot\boldsymbol{P}(\hat{\boldsymbol{r}})\frac{e^{-jkr}}{kr}(1 + \mathcal{O}((kr)^{-1}))\right]\\ &= \frac{1}{k}\hat{\boldsymbol{r}}\left[-j\hat{\boldsymbol{r}}\cdot\boldsymbol{P}(\hat{\boldsymbol{r}})(-jk - \frac{1}{r})\frac{e^{-jkr}}{kr}(1 + \mathcal{O}((kr)^{-1}))\right]\\ &= -\hat{\boldsymbol{r}}\left[\hat{\boldsymbol{r}}\cdot\boldsymbol{P}(\hat{\boldsymbol{r}})\frac{e^{-jkr}}{kr}(1 + \mathcal{O}((kr)^{-1}))\right]\end{aligned}$$

Hence, the operator $\mathcal{L}$ may be rewritten as

$$\begin{aligned}(\mathcal{L}\boldsymbol{X})(\boldsymbol{r}) &= \left[\boldsymbol{P}(\hat{\boldsymbol{r}}) - \hat{\boldsymbol{r}}(\hat{\boldsymbol{r}}\cdot\boldsymbol{P}(\hat{\boldsymbol{r}}))\right]\frac{e^{-jkr}}{kr}\\ &= -\hat{\boldsymbol{r}}\times(\hat{\boldsymbol{r}}\times\boldsymbol{P}(\hat{\boldsymbol{r}}))\frac{e^{-jkr}}{kr},\end{aligned} \tag{A.7}$$

where we have used $r \gg \lambda$.

Following the above example for the operator $\mathcal{K}$, we have

$$\begin{aligned}(\mathcal{K}\boldsymbol{X})(\boldsymbol{r}) &= \nabla \times \int_S G(\boldsymbol{r}, \boldsymbol{r}')\boldsymbol{X}(\boldsymbol{r}')\,\mathrm{d}S's \\ &= \frac{1}{k}\nabla \times \left[\frac{e^{-jkr}}{kr}\boldsymbol{P}(\hat{\boldsymbol{r}})\right].\end{aligned}$$

Evaluating the cross product in spherical coordinates gives

$$\begin{aligned}\frac{1}{k}\nabla \times \left[\frac{e^{-jkr}}{kr}\boldsymbol{P}(\hat{\boldsymbol{r}})\right] &= \frac{1}{k}\left[\frac{e^{-jkr}}{kr}\nabla \times \boldsymbol{P}(\hat{\boldsymbol{r}}) + \nabla\left(\frac{e^{-jkr}}{kr}\right) \times \boldsymbol{P}(\hat{\boldsymbol{r}})\right] \\ &= \frac{e^{-jkr}}{(kr)^2}\left[\hat{\boldsymbol{r}}\frac{1}{\sin\theta}\left(\frac{\partial(P_\phi \sin\theta)}{\partial\theta} - \frac{\partial P_\theta}{\partial\phi}\right) + \hat{\boldsymbol{\theta}}\frac{1}{\sin\theta}\frac{\partial P_r}{\partial\phi} - \hat{\boldsymbol{\phi}}\frac{\partial P_r}{\partial\theta}\right] \\ &+ \left[\hat{\boldsymbol{r}}\frac{1}{k}\left(-jk - \frac{1}{r}\right)\frac{e^{-jkr}}{kr}\right] \times \boldsymbol{P}(\hat{\boldsymbol{r}}) \\ &= -j\hat{\boldsymbol{r}} \times \boldsymbol{P}(\hat{\boldsymbol{r}})\frac{e^{-jkr}}{kr}(1 + \mathcal{O}((kr)^{-1})).\end{aligned}$$

Using $r \gg \lambda$, we finally arrive at

$$(\mathcal{K}\boldsymbol{X})(\boldsymbol{r}) = -j\hat{\boldsymbol{r}} \times \boldsymbol{P}(\hat{\boldsymbol{r}})\frac{e^{-jkr}}{kr}. \tag{A.8}$$

It is clear from (A.7) and (A.8) that the dominating term scales as $1/r$ and that the far-fields possess no components in the direction of propagation $\hat{\boldsymbol{r}}$ outward from the scatterer.

Appendix B

Projection point on tangent plane

Assume we have a curved surface described by the mapping $\boldsymbol{r}(u, v)$. A first-order Taylor approximation of the curved surface around the point (u_0, v_0) is described by

$$\boldsymbol{r}_{\text{lin}}(u, v) = \boldsymbol{r}_0 + \boldsymbol{a}_0(u - u_0) + \boldsymbol{b}_0(v - v_0), \tag{B.1}$$

where $\boldsymbol{r}_0 = \boldsymbol{r}(u_0, v_0)$ and $\boldsymbol{a}_0 = \frac{\partial \boldsymbol{r}}{\partial u}\Big|_{(u_0,v_0)}$, $\boldsymbol{b}_0 = \frac{\partial \boldsymbol{r}}{\partial v}\Big|_{(u_0,v_0)}$ are the co-variant basis vectors. Given a known field point $\boldsymbol{r}_{\text{f}}$, the projected point $\boldsymbol{r}_{\text{p}} = \boldsymbol{r}(u_{\text{p}}, v_{\text{p}})$ of $\boldsymbol{r}_{\text{f}}$ onto the linearized surface $\boldsymbol{r}_{\text{lin}}(u, v)$ is found by minimizing the cost function

$$g(u, v) = |\boldsymbol{r}_{\text{lin}}(u, v) - \boldsymbol{r}_{\text{f}}|^2 = |\boldsymbol{r}_{\text{lin}}(u, v)|^2 - 2\boldsymbol{r}_{\text{lin}}(u, v)\boldsymbol{r}_{\text{f}} + |\boldsymbol{r}_{\text{f}}|^2. \tag{B.2}$$

The analytical solution is found by setting the partial derivatives to zero

$$\begin{cases} \frac{\partial g}{\partial u}\Big|_{(u_{\text{p}},v_{\text{p}})} = -2\boldsymbol{r}_{\text{f}} \cdot \boldsymbol{a}_0 + 2\boldsymbol{r}_{\text{lin}}(u_{\text{p}}, v_{\text{p}}) \cdot \boldsymbol{a}_0 = 2\boldsymbol{a}_0 \cdot (\boldsymbol{r}_{\text{lin}}(u_{\text{p}}, v_{\text{p}}) - \boldsymbol{r}_{\text{f}}) = 0 \\ \frac{\partial g}{\partial v}\Big|_{(u_{\text{p}},v_{\text{p}})} = -2\boldsymbol{r}_{\text{f}} \cdot \boldsymbol{b}_0 + 2\boldsymbol{r}_{\text{lin}}(u_{\text{p}}, v_{\text{p}}) \cdot \boldsymbol{b}_0 = 2\boldsymbol{b}_0 \cdot (\boldsymbol{r}_{\text{lin}}(u_{\text{p}}, v_{\text{p}}) - \boldsymbol{r}_{\text{f}}) = 0 \end{cases}, \tag{B.3}$$

$$\begin{cases} \boldsymbol{a}_0 \cdot (\boldsymbol{r}_0 + \boldsymbol{a}_0(u_{\text{p}} - u_0) + \boldsymbol{b}_0(v_{\text{p}} - v_0) - \boldsymbol{r}_{\text{f}}) = 0 \\ \boldsymbol{b}_0 \cdot (\boldsymbol{r}_0 + \boldsymbol{a}_0(u_{\text{p}} - u_0) + \boldsymbol{b}_0(v_{\text{ffl}p} - v_0) - \boldsymbol{r}_{\text{f}}) = 0 \end{cases}. \tag{B.4}$$

Inserting the expression for $\boldsymbol{r}_{\text{lin}}$ and collecting terms we arrive at the system of linear equations

$$\begin{bmatrix} |\boldsymbol{a}_0|^2 & \boldsymbol{a}_0 \cdot \boldsymbol{b}_0 \\ \boldsymbol{a}_0 \cdot \boldsymbol{b}_0 & |\boldsymbol{b}_0|^2 \end{bmatrix} \begin{bmatrix} u_{\text{p}} \\ v_{\text{p}} \end{bmatrix} = \begin{bmatrix} \boldsymbol{a}_0 \cdot (\boldsymbol{r}_{\text{f}} - \boldsymbol{r}_0 + \boldsymbol{a}_0 u_0 + \boldsymbol{b}_0 v_0) \\ \boldsymbol{b}_0 \cdot (\boldsymbol{r}_{\text{f}} - \boldsymbol{r}_0 + \boldsymbol{a}_0 u_0 + \boldsymbol{b}_0 v_0) \end{bmatrix}, \tag{B.5}$$

where $(u_{\text{p}}, v_{\text{p}})$ is the solution.

Appendix C

Strong true singularity treatment

Consider the integral

$$\boldsymbol{I}(\boldsymbol{r}) = \int_S \nabla G(\boldsymbol{r}, \boldsymbol{r}') \nabla' \cdot \boldsymbol{X}(\boldsymbol{r}') \, \mathrm{d}S', \tag{C.1}$$

where we have a true strong singularity located on the surface S. In the following, we denote $\nabla' \cdot \boldsymbol{X}(\boldsymbol{r}') = s(\boldsymbol{r}')$. Then

$$\begin{aligned}
\boldsymbol{I}(\boldsymbol{r}) &= -\int_S \nabla \left(\frac{e^{-jk|\boldsymbol{r}-\boldsymbol{r}'|}}{4\pi|\boldsymbol{r}-\boldsymbol{r}'|} \right) s(\boldsymbol{r}') \, \mathrm{d}S' \\
&= \int_S \left[\frac{(1+jk|\boldsymbol{r}-\boldsymbol{r}'|e^{-jk|\boldsymbol{r}-\boldsymbol{r}'|}}{4\pi|\boldsymbol{r}-\boldsymbol{r}'|^2} \frac{\boldsymbol{r}-\boldsymbol{r}'}{|\boldsymbol{r}-\boldsymbol{r}'|} \right] s(\boldsymbol{r}') \, \mathrm{d}S' \\
&= \begin{cases} R = |\boldsymbol{r}-\boldsymbol{r}'| \\ \hat{\boldsymbol{R}} = (\boldsymbol{r}-\boldsymbol{r}')/|\boldsymbol{r}-\boldsymbol{r}'| \end{cases} \\
&= \int_{S_1} \left[\frac{(1+jkRe^{-jkR}}{4\pi R^2} \hat{\boldsymbol{R}} \right] s(\boldsymbol{r}') \, \mathrm{d}S' \\
&+ \int_{S_2} \left[\frac{(1+jkRe^{-jkR}}{4\pi R^2} \hat{\boldsymbol{R}} \right] s(\boldsymbol{r}') \, \mathrm{d}S' \\
&= \boldsymbol{I}_1(\boldsymbol{r}) + \boldsymbol{I}_2(\boldsymbol{r})
\end{aligned}$$

where S_2 is a disk with the center located at the singulary and with radius ϵ, and $S_1 = S \cap S_2$. Assume that ϵ is so small that S_2 is flat and perform integration in cylindrical coordinates. Also, assume that ϵ is sufficiently small to assume statics,

i.e $kR \to 0$ so that $1 + jkR \to 1$ and $e^{-jkR} \to 1$.

$$\begin{aligned}
\boldsymbol{I}_2(\boldsymbol{r}) &\simeq \int_{S_2} \left[\frac{1}{4\pi R^2}\hat{\boldsymbol{R}}\right] s(\boldsymbol{r}')\,\mathrm{d}S' \\
&= \{\rho(\boldsymbol{r}') \simeq \text{constant on } S_2 \Rightarrow s(\boldsymbol{r})\} \\
&\simeq \frac{\rho(\boldsymbol{r})}{4\pi}\int_{\phi'=0}^{2\pi}\int_{r'=0}^{\epsilon}\left[\frac{-\hat{\boldsymbol{r}}(\phi')r' + \hat{\boldsymbol{z}}z}{[(r')^2+z^2]^{3/2}}\right] r'\mathrm{d}r'\mathrm{d}\phi' \\
&= \frac{\rho(\boldsymbol{r})}{2}\int_{r'=0}^{\epsilon}\frac{\hat{\boldsymbol{z}}zr'}{[(r')^2+z^2]^{3/2}}\mathrm{d}r' \\
&= \frac{\rho(\boldsymbol{r})}{2}\hat{\boldsymbol{z}}z\left(\frac{1}{z} - \frac{1}{\sqrt{\epsilon^2+z^2}}\right) \\
\lim_{\epsilon\to 0}\boldsymbol{I}_2(\boldsymbol{r}) &= \frac{s(\boldsymbol{r})}{2}\hat{\boldsymbol{z}} = \frac{s(\boldsymbol{r})}{2}\hat{\boldsymbol{n}}
\end{aligned}$$

We are left with

$$\boldsymbol{I}(\boldsymbol{r}) = \int_{S_1}\left[\frac{(1+jkR)e^{-jkR}}{4\pi R^2}\hat{\boldsymbol{R}}\right] s(\boldsymbol{r}')\,\mathrm{d}S' + \frac{s(\boldsymbol{r})}{2}\hat{\boldsymbol{n}} \tag{C.2}$$

For S_1, we use the mapping $\boldsymbol{r}(u,v)$ described in (2.22) with corresponding covariant basis vectors $\boldsymbol{a}$, $\boldsymbol{b}$ (2.28) and $D(u,v) = |\boldsymbol{a}\times\boldsymbol{b}|$. Let (u_0, v_0) be centered at S_2 and use the polar coordinates defined by

$$\begin{aligned}
u &= u_0 + \rho\cos\phi \\
v &= v_0 + \rho\sin\phi
\end{aligned}$$

The excluded area S_2 is bounded by $|\boldsymbol{r}(u,v) - \boldsymbol{r}(u_0,v_0)| = \epsilon$. Since ϵ is very small, we can use Taylor expansion

$$\begin{aligned}
\boldsymbol{r}(u,v) &= \boldsymbol{r}(u_0,v_0) + \frac{\partial\boldsymbol{r}}{\partial u}\Big|_{(u_0,v_0)}(u-u_0) + \frac{\partial\boldsymbol{r}}{\partial v}\Big|_{(u_0,v_0)}(v-v_0)\ldots \\
\Rightarrow |\boldsymbol{r}(u,v) - \boldsymbol{r}(u_0,v_0)| &\simeq |\boldsymbol{a}_0(u-u_0) + \boldsymbol{b}_0(v-v_0)| \\
&= |\boldsymbol{a}_0\rho\cos\phi + \boldsymbol{b}_0\rho\sin\phi| \\
&= \rho|\boldsymbol{a}_0\cos\phi + \boldsymbol{b}_0\sin\phi| = \epsilon.
\end{aligned}$$

Thus, we have S_2 described by

$$\rho_\epsilon \le \frac{\epsilon}{|\boldsymbol{a}_0\cos\phi + \boldsymbol{b}_0\sin\phi|}. \tag{C.3}$$

The outer boundary is described in terms of straight line segments form a point (u_1, v_1) to another point (u_2, v_2), which gives at the boundary

$$\beta(\xi) = \xi(u_1,v_1) + (1-\xi)(u_2,v_2) \text{ for } 0 \le \xi \le 1.$$

$$\begin{cases}
p(\xi) = \xi u_1 + (1-\xi)u_2 - u_0 = \rho\cos\phi \\
q(\xi) = \xi v_1 + (1-\xi)v_2 - v_0 = \rho\sin\phi
\end{cases}$$

$$\begin{cases} \rho_\beta(\xi) = \sqrt{p^2(\xi) + q^2(\xi)} \\ \phi(\xi) = \arctan(p(\xi)/\sqrt{p^2(\xi) + q^2(\xi)}) \end{cases}$$

or

$$\begin{cases} \rho_\beta(\phi) = \frac{u_0(v_1-v_2)+u_1(v_2-v_0)+u_2(v_0-v_1)}{(v_2-v_1)\cos\phi+(u_1-u_2)\sin\phi} \\ \xi(\phi) = \frac{(v_2-v_0)\cos\phi+(u_0-u_2)\sin\phi}{(v_2-v_1)\cos\phi+(u_1-u_2)\sin\phi} \end{cases},$$

which is useful in the following. We now have

$$\begin{aligned} \boldsymbol{I}_1(\boldsymbol{r}) &= \int_{S_1} \left[\frac{(1+jkR)e^{-jkR}}{4\pi R^2} \hat{\boldsymbol{R}} \right] s(\boldsymbol{r}')\, \mathrm{d}S' \\ &= \int_{\phi'=0}^{2\pi} \int_{\rho'_\epsilon(\phi')}^{\rho'_\beta(\phi')} \left[\frac{(1+jkR)e^{-jkR}}{4\pi R^2} \hat{\boldsymbol{R}} \right] s(\boldsymbol{r}') D(u',v') \rho'\, \mathrm{d}\rho' \mathrm{d}\phi' \\ &= \left\{ \boldsymbol{\Gamma}(u',v') = \boldsymbol{\Gamma}(\rho',\phi') = \left[\frac{(1+jkR)e^{-jkR}}{4\pi R^2} \hat{\boldsymbol{R}} \right] s(\boldsymbol{r}') D(u',v') \rho' \right\} \\ &= \int_{\phi'=0}^{2\pi} \int_{\rho'_\epsilon(\phi')}^{\rho'_\beta(\phi')} \boldsymbol{\Gamma}(\rho',\phi')\, \mathrm{d}\rho' \mathrm{d}\phi' \end{aligned}$$

where

$$\begin{cases} \boldsymbol{r} = \boldsymbol{r}(u_0, v_0) \\ \boldsymbol{r}' = \boldsymbol{r}(u', v') \\ R = |\boldsymbol{r}(u_0, v_0) - \boldsymbol{r}(u', v')| \\ \hat{\boldsymbol{R}} = (\boldsymbol{r}(u_0, v_0) - \boldsymbol{r}(u', v'))/|\boldsymbol{r}(u_0, v_0) - \boldsymbol{r}(u', v')|. \end{cases}$$

The integrand $\boldsymbol{\Gamma}$ exhibits a weak singularity ($\propto 1/\rho'$) as the point (u_0, v_0) is approached. The proportionality constant for the part of the integrand that scales as $1/\rho$ is given by

$$\boldsymbol{\gamma}(\phi') = \lim_{\rho' \to 0} \rho' \boldsymbol{\Gamma}(\rho', \phi')$$

$$= \begin{cases} \hat{\boldsymbol{R}} = \frac{\boldsymbol{r}(u_0,v_0)-\boldsymbol{r}(u',v')}{|\boldsymbol{r}(u_0,v_0)-\boldsymbol{r}(u',v')|} = \frac{\hat{\boldsymbol{U}}_0(u_0-u')+\hat{\boldsymbol{V}}_0(v_0-v')}{|\hat{\boldsymbol{U}}_0(u_0-u')+\hat{\boldsymbol{V}}_0(v_0-v')|} \\ R = |\boldsymbol{r}(u_0, v_0) - \boldsymbol{r}(u', v')| = |\hat{\boldsymbol{U}}_0(u_0 - u') + \hat{\boldsymbol{V}}_0(v_0 - v')| \\ \text{Static approx:} (1 + jkR) \to 1 \text{ and } e^{-jkR} \to 1 \end{cases}$$

$$\begin{aligned} &= \lim_{\rho' \to 0} \frac{-(\boldsymbol{a}_0(u_0 - u') + \boldsymbol{b}_0(v_0 - v'))}{4\pi |\boldsymbol{a}_0(u_0 - u') + \boldsymbol{b}_0 0(v_0 - v')|^3} s(\boldsymbol{r'}) D(u', v') (\rho')^2 \\ &= \lim_{\rho' \to 0} \frac{-(\rho'(\boldsymbol{a}_0 \cos\phi' + \boldsymbol{b}_0 0 \sin\phi'))}{4\pi (\rho')^3 |\boldsymbol{a}_0 \cos\phi' + \boldsymbol{b}_0 \sin\phi'|^3} s(\boldsymbol{r'}) D(u', v') (\rho')^2 \\ &= \frac{1}{4\pi} \frac{-(\boldsymbol{a}_0 \cos\phi' + \boldsymbol{b}_0 \sin\phi')}{|\boldsymbol{a}_0 \cos\phi' + \boldsymbol{b}_0 \sin\phi'|^3} s(\boldsymbol{r'}(u_0, v_0)) D(u_0, v_0). \end{aligned}$$

Thus, we have

$$\begin{aligned}\boldsymbol{I}_1(\boldsymbol{r}) &= \int_{\phi'=0}^{2\pi}\int_{\rho'_\epsilon(\phi')}^{\rho'_\beta(\phi')}\left(\boldsymbol{\Gamma}(\rho',\phi') - \frac{\boldsymbol{\gamma}(\phi')}{\rho'}\right)\mathrm{d}\rho'\mathrm{d}\phi' \\ &\quad + \int_{\phi'=0}^{2\pi}\int_{\rho'_\epsilon(\phi')}^{\rho'_\beta(\phi')}\frac{\boldsymbol{\gamma}(\phi')}{\rho'}\,\mathrm{d}\rho'\mathrm{d}\phi' \\ &= \boldsymbol{I}_1^{\mathrm{reg}}(\boldsymbol{r}) + \boldsymbol{I}_1^{\mathrm{sing}}(\boldsymbol{r}),\end{aligned}$$

where

$$\begin{aligned}\boldsymbol{I}_1^{\mathrm{sing}}(\boldsymbol{r}) &= \int_{\phi'=0}^{2\pi}\boldsymbol{\gamma}(\phi')\ln\left(\frac{\rho'_\beta(\phi')}{\rho'_\epsilon(\phi')}\right)\mathrm{d}\phi' \\ &= \int_{\phi'=0}^{2\pi}\boldsymbol{\gamma}(\phi')\ln\left(\rho'_\beta(\phi')\frac{|\boldsymbol{a}_0\cos\phi + \boldsymbol{b}_0\sin\phi|}{\epsilon}\right)\mathrm{d}\phi' \\ &= \int_{\phi'=0}^{2\pi}\boldsymbol{\gamma}(\phi')\ln\left(\rho'_\beta(\phi')|\boldsymbol{a}_0\cos\phi + \boldsymbol{b}_0\sin\phi|\right)\mathrm{d}\phi' - \ln\epsilon\int_{\phi'=0}^{2\pi}\boldsymbol{\gamma}(\phi')\,\mathrm{d}\phi' \\ &= \int_{\phi'=0}^{2\pi}\boldsymbol{\gamma}(\phi')\ln\left(\rho'_\beta(\phi')|\boldsymbol{a}_0\cos\phi + \boldsymbol{b}_0\sin\phi|\right)\mathrm{d}\phi',\end{aligned}$$

where the last integral vanished since $\boldsymbol{\gamma}(\boldsymbol{r}')$ is periodic on the interval $[0, 2\pi]$ with a zero mean. Finally, we get (when $\epsilon \to 0^+$)

$$\begin{aligned}\boldsymbol{I}(\boldsymbol{r}) &= \int_{\phi'=0}^{2\pi}\int_{\rho'_\epsilon(\phi')\to 0^+}^{\rho'_\beta(\phi')}\left(\boldsymbol{\Gamma}(\rho',\phi') - \frac{\boldsymbol{\gamma}(\phi')}{\rho'}\right)\mathrm{d}\rho'\mathrm{d}\phi' \\ &\quad + \int_{\phi'=0}^{2\pi}\boldsymbol{\gamma}(\phi')\ln\left(\rho'_\beta(\phi')|\boldsymbol{a}_0\cos\phi + \boldsymbol{b}_0\sin\phi|\right)\mathrm{d}\phi' \\ &\quad + \frac{s(\boldsymbol{r})}{2}.\end{aligned}$$

The first term in the above expression is regular because $\boldsymbol{\gamma}$ is defined as: $\boldsymbol{\gamma}(\phi) = \lim_{\rho\to 0}\rho\boldsymbol{\Gamma}(\rho,\phi)$, and may be integrated with direct Gaussian quadrature. The second term is a regular contour integral and the last term is the Cauchy principal value term.

Appendix D

Analytic solutions for a test problem

Consider a sphere of radius a with surface currents $\boldsymbol{J}$ and $\boldsymbol{M}$. For $r > a$, the electromagnetic field from one mode in the multipole expansion are given in spherical coordinates as

$$\boldsymbol{E}(r,\theta,\phi) = \sqrt{\frac{3}{2\pi}}\frac{\mathbf{E}_0}{kr}\left[\hat{\boldsymbol{r}}h_1^{(2)}(kr)\cos(\theta) + \hat{\boldsymbol{\theta}}\frac{1}{2}\left(h_1^{(2)}(kr) - krh_0^{(2)}(kr)\right)\sin(\theta)\right], \tag{D.1}$$

$$\boldsymbol{H}(r,\theta,\phi) = -\hat{\boldsymbol{\phi}}\sqrt{\frac{3}{2\pi}}\frac{\mathbf{E}_0}{2Z_0}\frac{1+jkr}{(kr)^2}e^{-jkr}\sin(\theta), \tag{D.2}$$

where $h_1^{(2)}$, $h_0^{(2)}$ are spherical Hankel functions of second kind. Further, we let $\boldsymbol{E} = \mathbf{0}$ and $\boldsymbol{H} = \mathbf{0}$ for $r < a$. Thus, we may calculate the currents $\boldsymbol{J}$ and $\boldsymbol{M}$ on the surface $r = a$ from the boundary conditions,

$$-\hat{\boldsymbol{n}} \times \boldsymbol{E}_1 = \boldsymbol{M}_s, \tag{D.3}$$

$$\hat{\boldsymbol{n}} \times \boldsymbol{H}_1 = \boldsymbol{J}_s, \tag{D.4}$$

$$\hat{\boldsymbol{n}} \cdot \boldsymbol{D}_1 = \rho_s, \tag{D.5}$$

$$\hat{\boldsymbol{n}} \cdot \boldsymbol{B}_1 = \varrho_s. \tag{D.6}$$

On the surface $r = a$ of the sphere, we have $\hat{\boldsymbol{n}} = \hat{\boldsymbol{r}}$ and Eqs. (D.3) and (D.4) yield

$$\boldsymbol{J}_s(\theta,\phi) = \hat{\boldsymbol{\theta}}\sqrt{\frac{3}{2\pi}}\frac{\mathbf{E}_0}{2Z_0}\frac{1+jka}{(ka)^2}e^{-jka}\sin(\theta), \tag{D.7}$$

$$\boldsymbol{M}_s(\theta,\phi) = \hat{\boldsymbol{\phi}}\sqrt{\frac{3}{2\pi}}\frac{\mathbf{E}_0}{ka}\left[\frac{1}{2}\left(kah_0^{(2)}(ka) - h_1^{(2)}(ka)\right)\sin(\theta)\right], \tag{D.8}$$

where we have used the expressions for the scattered fields (D.1), (D.2) and the relations $\hat{\boldsymbol{r}} \times \hat{\boldsymbol{r}} = 0$, $\hat{\boldsymbol{r}} \times \hat{\boldsymbol{\theta}} = \hat{\boldsymbol{\phi}}$.